

# **Introduction to Nuclear and Particle Physics**

**Nuclear structure - nuclear force**

**Helga Dénés 2022 Yachay Tech**

[hdenes@yachaytech.edu.ec](mailto:hdenes@yachaytech.edu.ec)

# Nucleon excited states

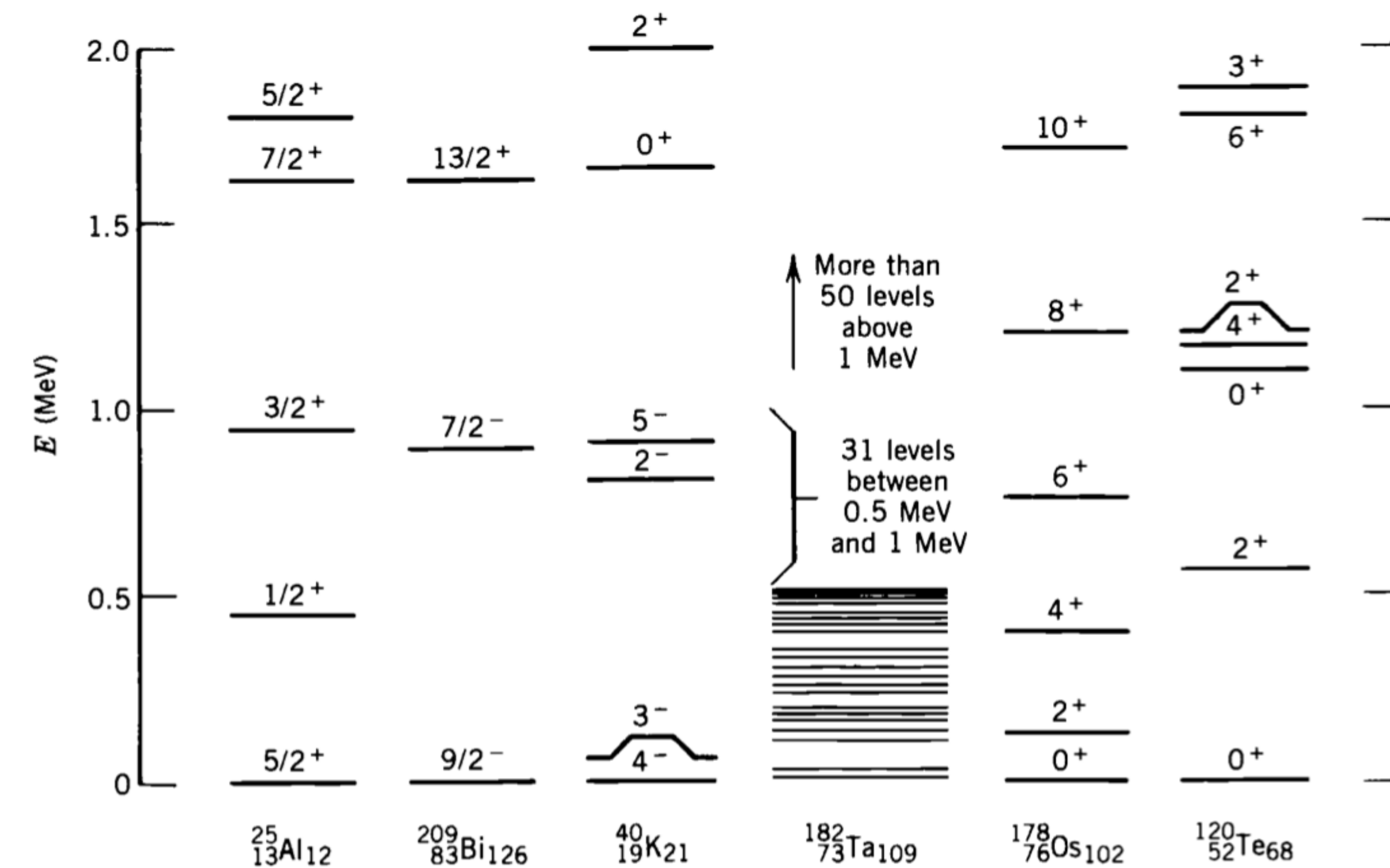


**Figure 3.19** Some sample level schemes showing the excited states below 2 MeV. Some nuclei, such as  $^{209}\text{Bi}$ , show great simplicity, while others, such as  $^{182}\text{Ta}$ , show great complexity. There is a regularity associated with the levels of  $^{178}\text{Os}$  that is duplicated in all even- $Z$ , even- $N$  nuclei in the range  $150 \leq A \leq 190$ . Structures similar to  $^{120}\text{Te}$  are found in many nuclei in the range  $50 \leq A \leq 150$ .

# Deuteron

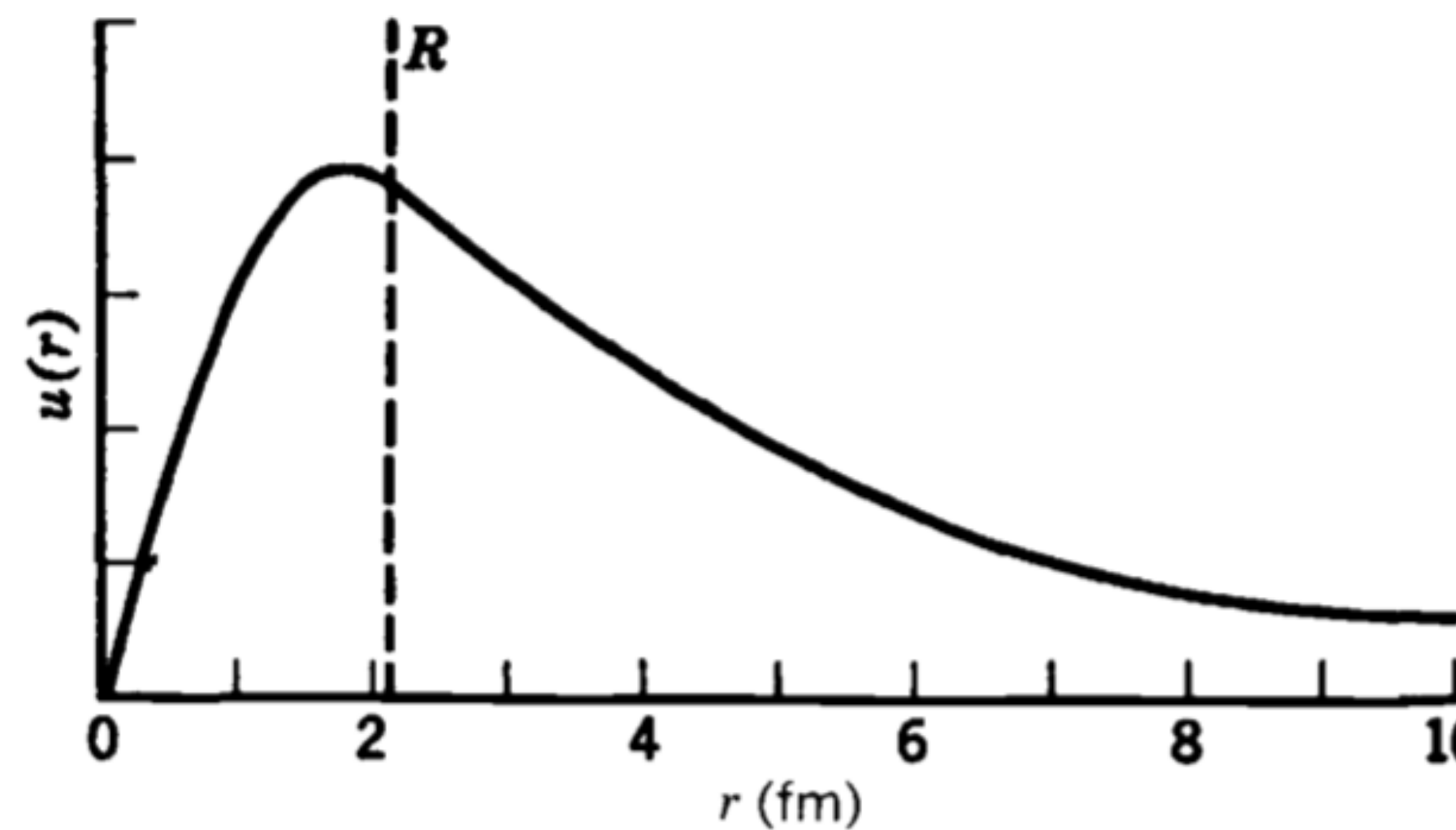


**Figure 4.2** The deuteron wave function for  $R = 2.1$  fm. Note how the exponential joins smoothly to the sine at  $r = R$ , so that both  $u(r)$  and  $du/dr$  are continuous. If the wave function did not “turn over” inside  $r = R$ , it would not be possible to connect smoothly to a decaying exponential (negative slope) and there would be no bound state.

# Diffraction

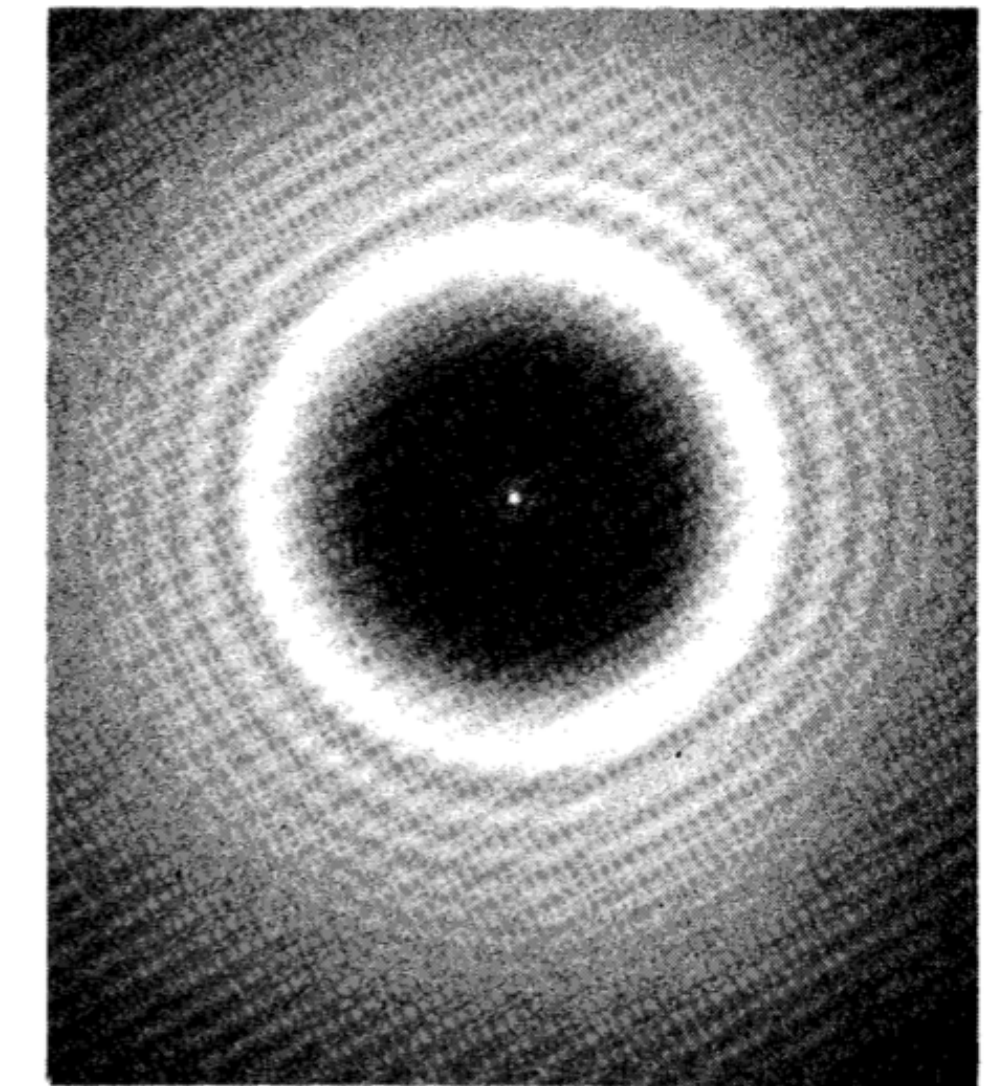
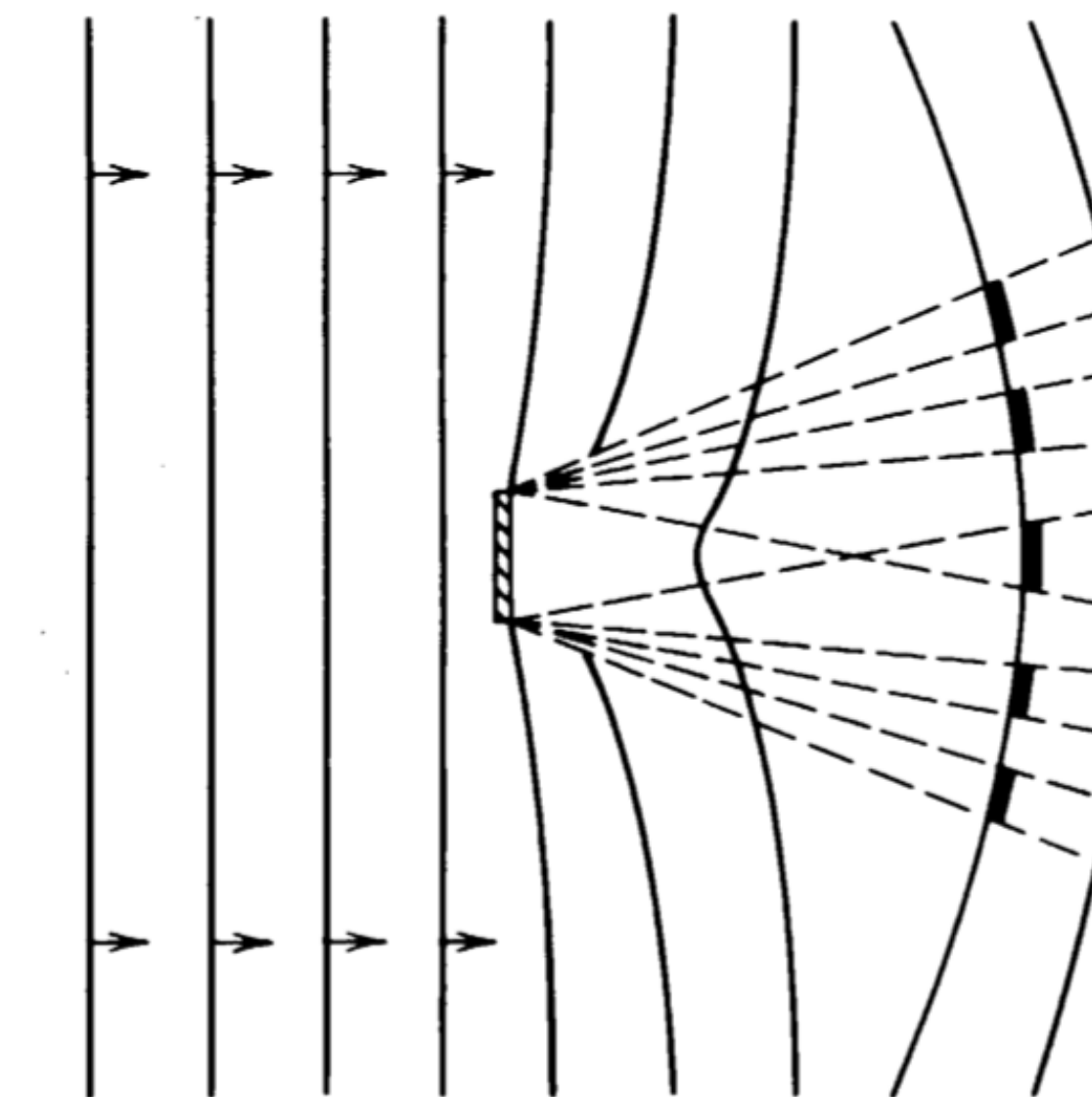
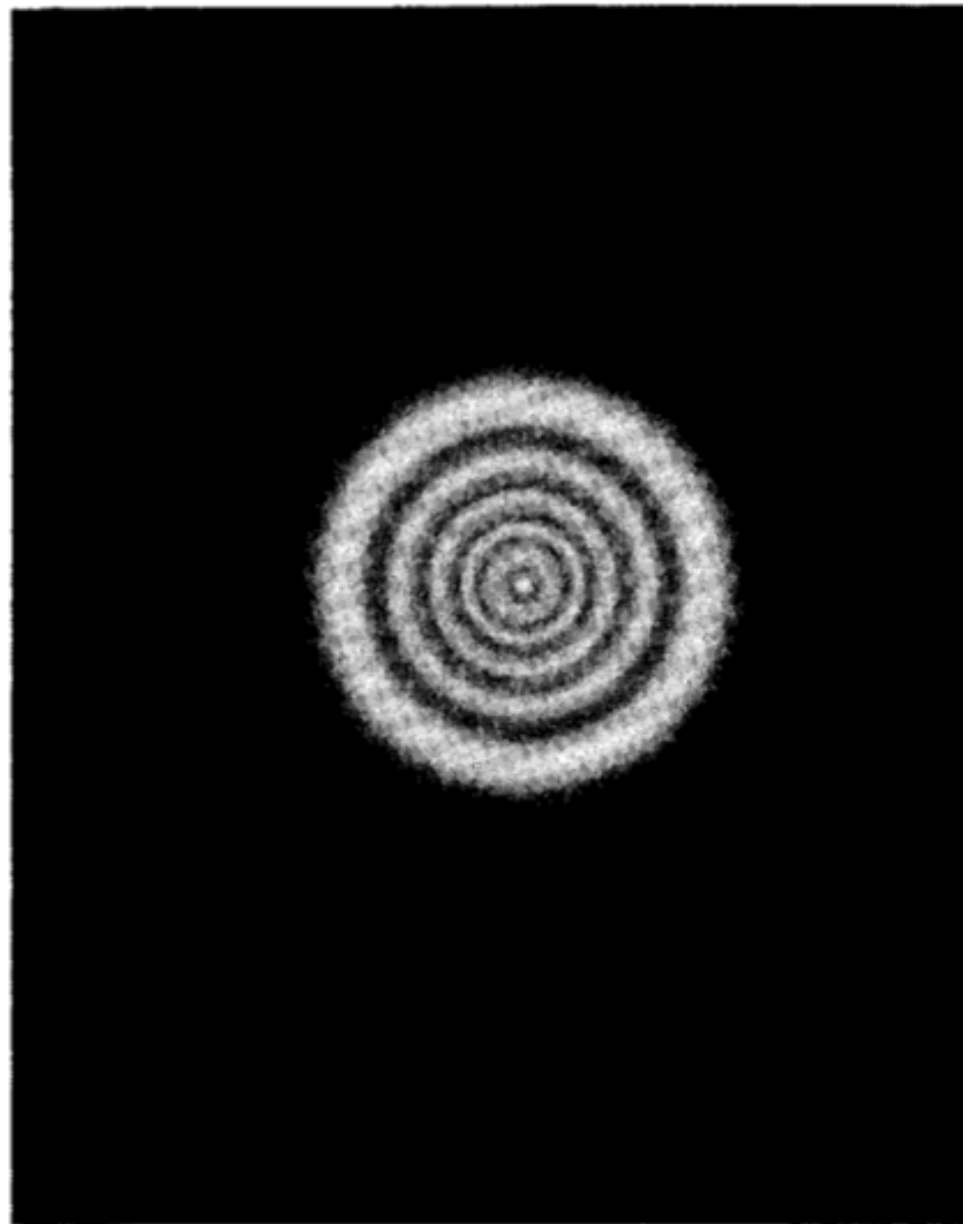
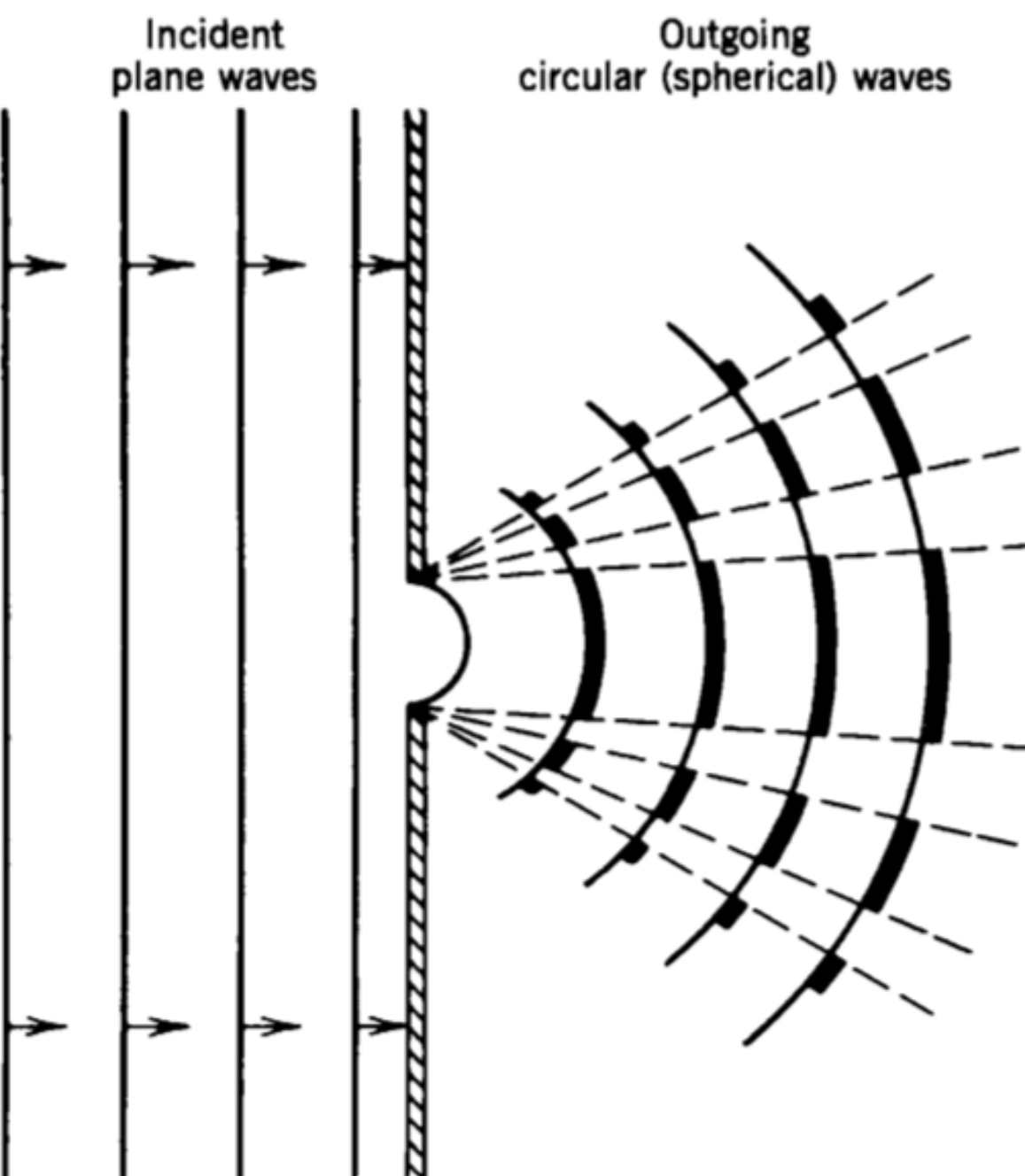


**Figure 4.3** Representation of scattering by (top) a small opening and (bottom) a small obstacle. The shading of the wavefronts shows regions of large and small intensity. On the right are shown photographs of diffraction by a circular opening and an opaque circular disk. Source of photographs: M. Cagnet, M. Francon, and J. C. Thrierr, *Atlas of Optical Phenomena* (Berlin: Springer-Verlag, 1962).

# Scattering

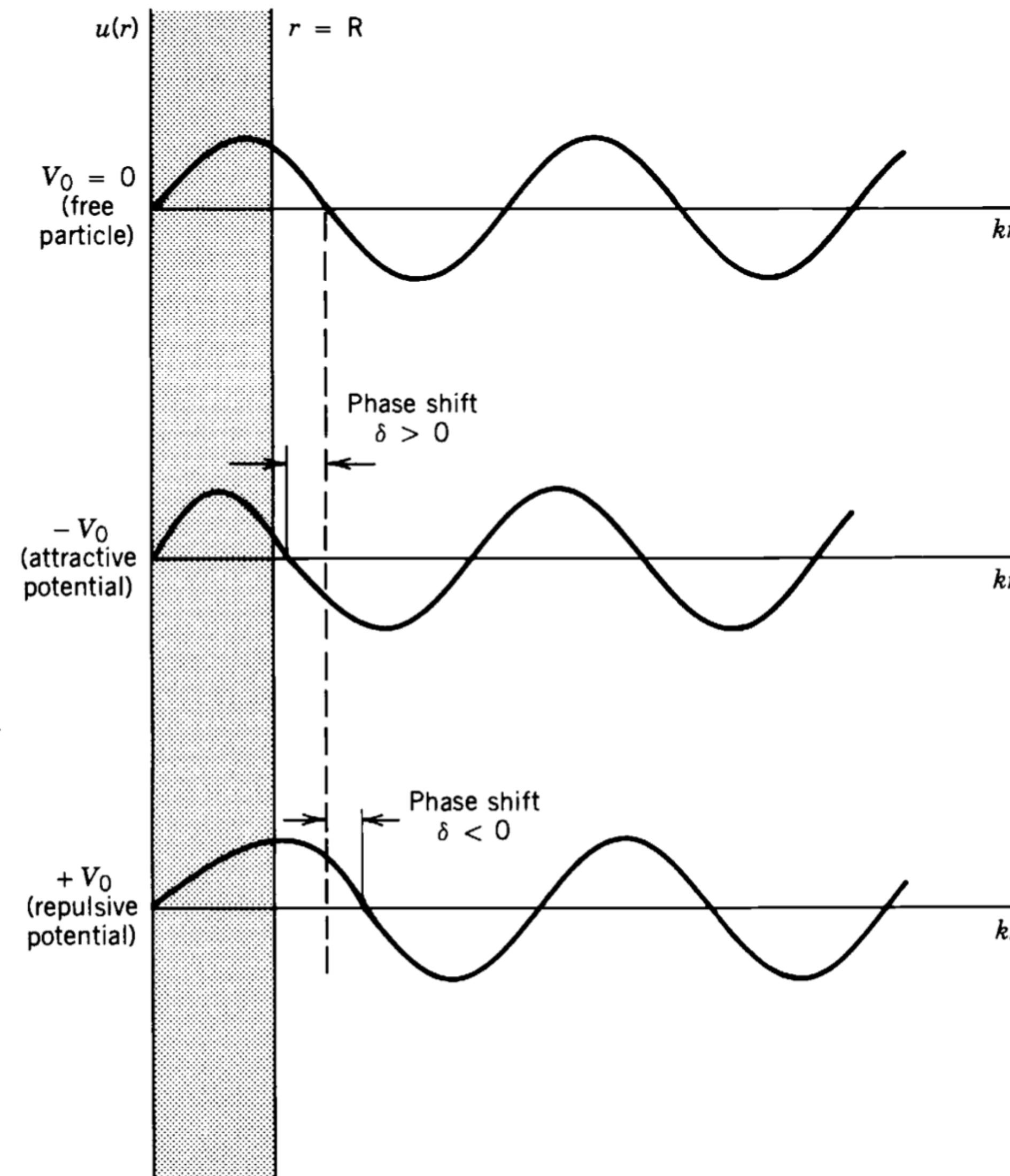


**Figure 4.4** The effect of a scattering potential is to shift the phase of the scattered wave at points beyond the scattering regions, where the wave function is that of a free particle.

# Scattering

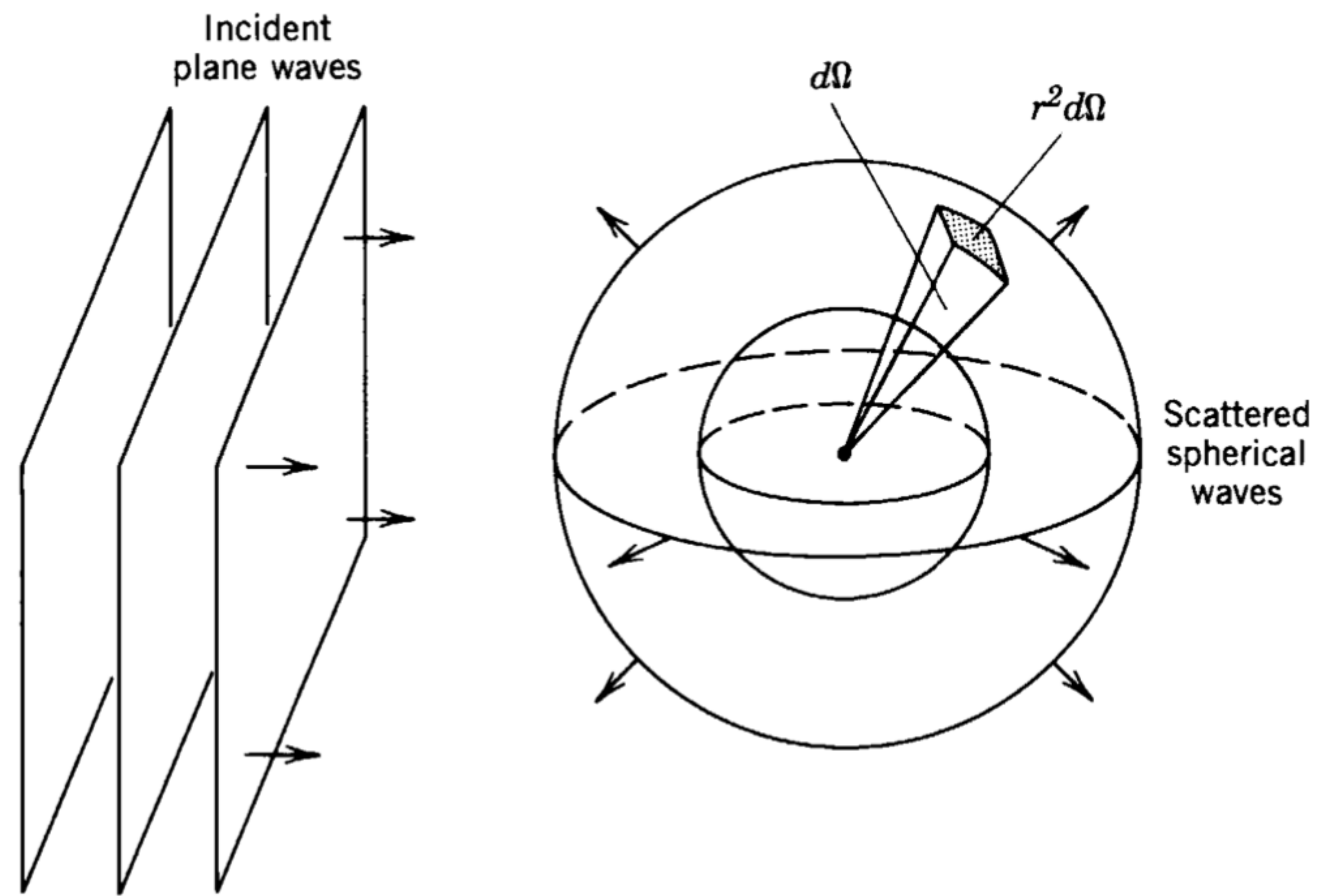


**Figure 4.5** The basic geometry of scattering.

# Scattering

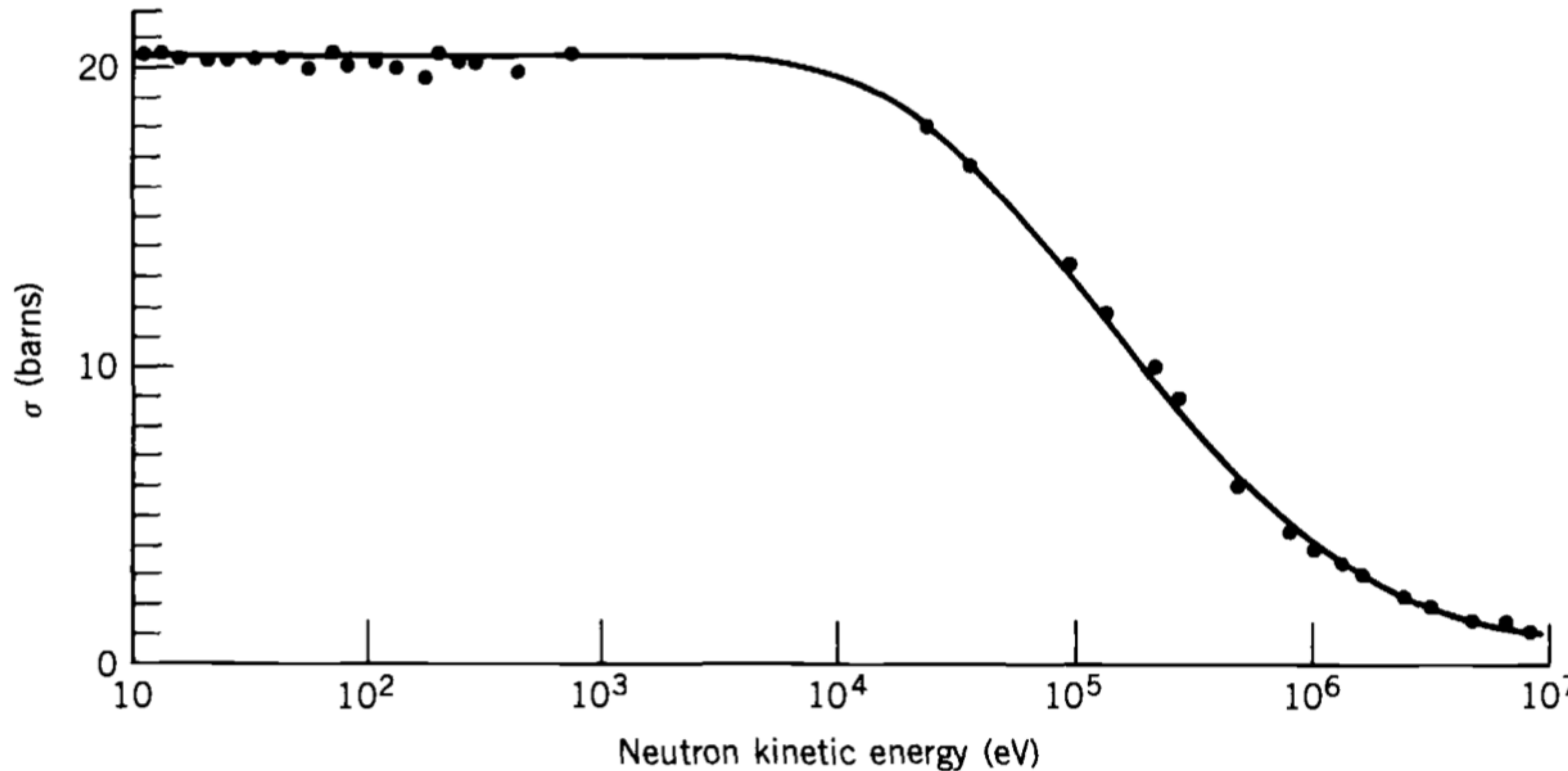


**Figure 4.6** The neutron–proton scattering cross section at low energy. Data taken from a review by R. K. Adair, *Rev. Mod. Phys.* **22**, 249 (1950), with additional recent results from T. L. Houk, *Phys. Rev. C* **3**, 1886 (1970).

# Scattering

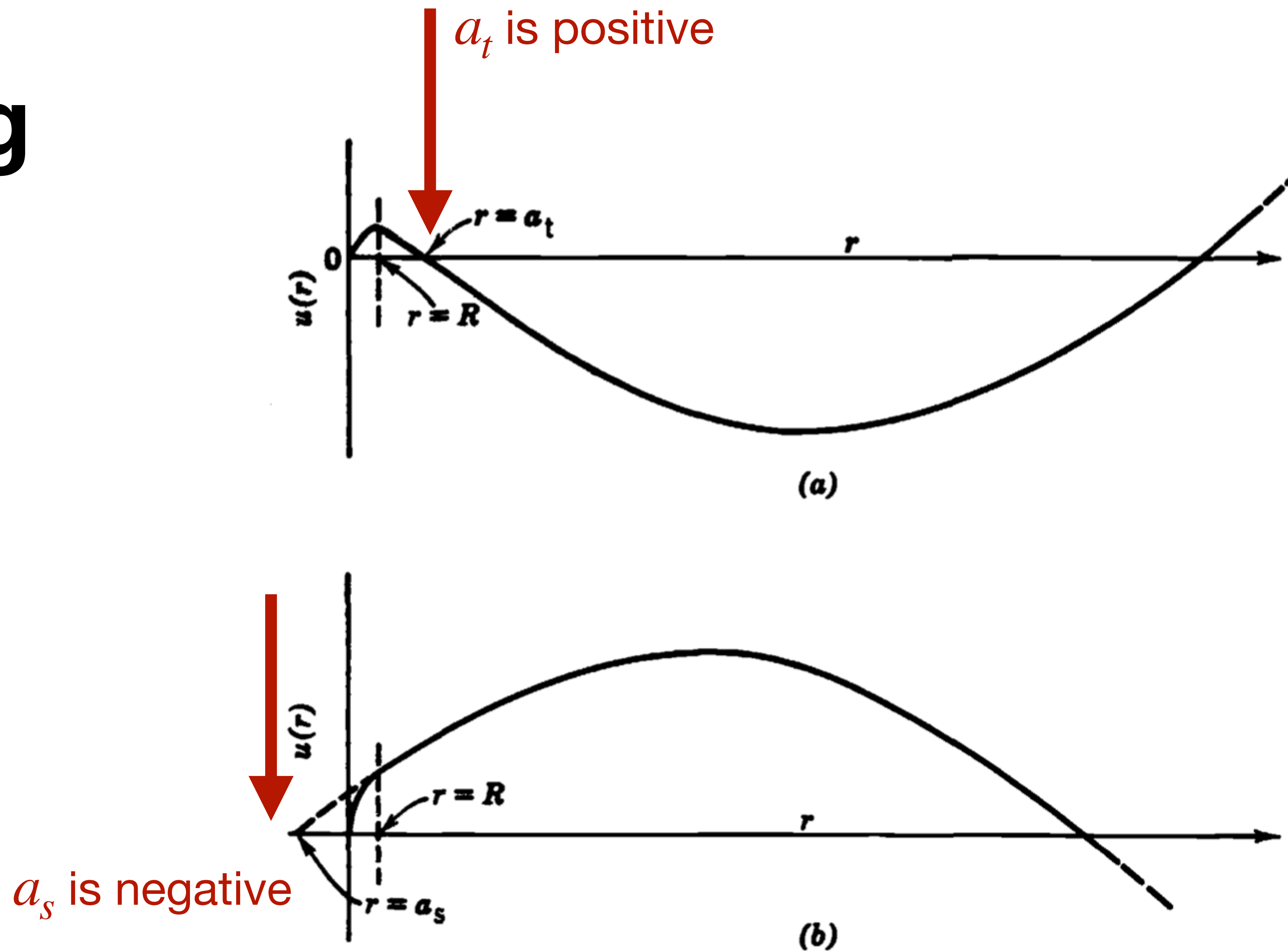


**Figure 4.7** (a) Wave function for triplet np scattering for a laboratory neutron energy of  $\sim 200$  keV and a well radius of 2.1 fm. Note the positive scattering length. (b) Wave function exhibiting a negative scattering length. This happens to be the case for singlet np scattering.

# Scattering

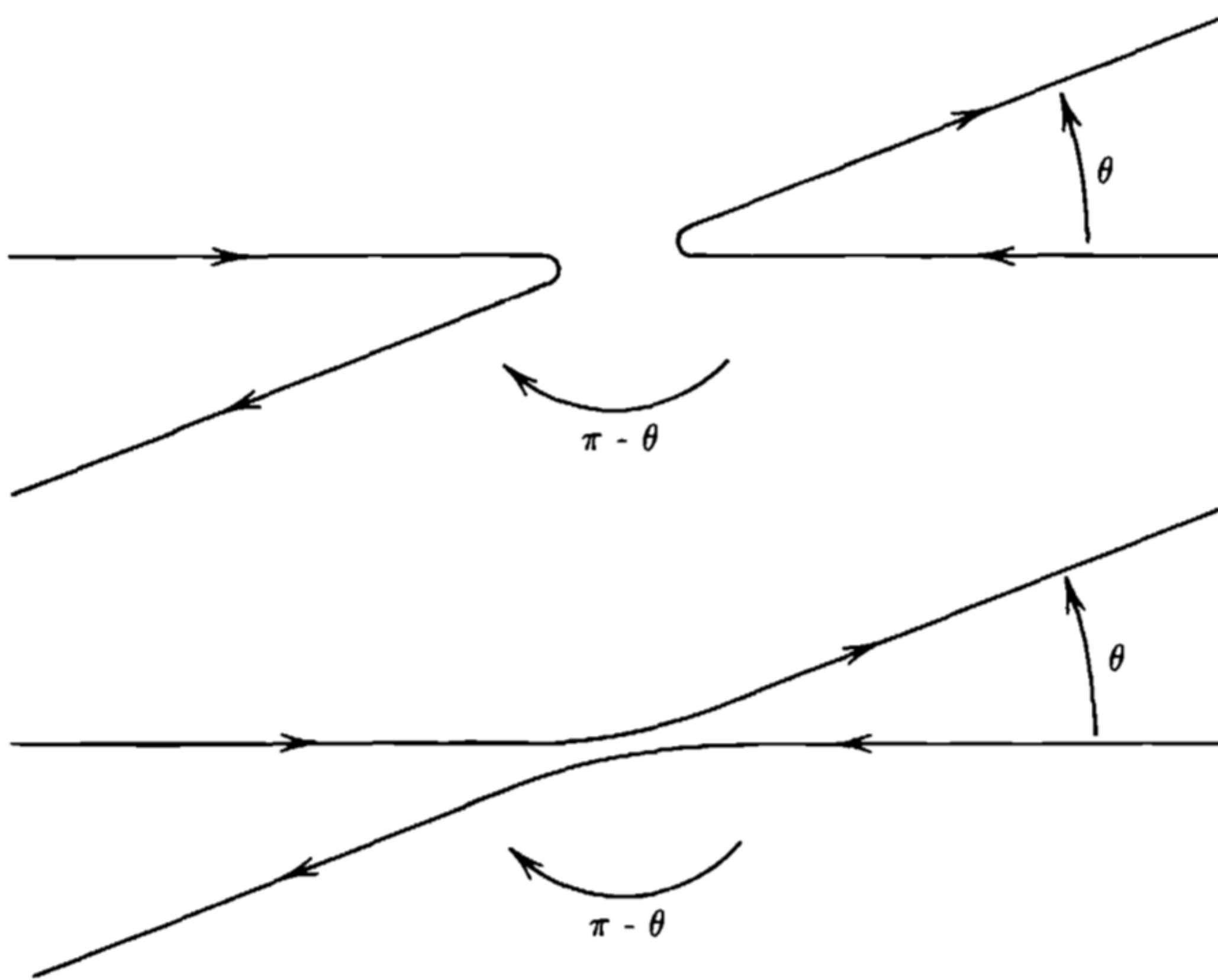


**Figure 4.8** Scattering of identical particles in the center-of-mass system. One particle emerges at the angle  $\theta$  and the other at  $\pi - \theta$ ; because the particles are identical, there is no way to tell which particle emerges at which angle, and therefore we cannot distinguish the two cases shown.

# p-p Scattering

$$\begin{aligned} \frac{d\sigma}{d\Omega} = & \left( \frac{e^2}{4\pi\epsilon_0} \right)^2 \frac{1}{4T^2} \left\{ \frac{1}{\sin^4(\theta/2)} + \frac{1}{\cos^4(\theta/2)} - \frac{\cos[\eta \ln \tan^2(\theta/2)]}{\sin^2(\theta/2) \cos^2(\theta/2)} \right. \\ & - \frac{2}{\eta} (\sin \delta_0) \left( \frac{\cos[\delta_0 + \eta \ln \sin^2(\theta/2)]}{\sin^2(\theta/2)} + \frac{\cos[\delta_0 + \eta \ln \cos^2(\theta/2)]}{\cos^2(\theta/2)} \right) \\ & \left. + \frac{4}{\eta^2} \sin^2 \delta_0 \right\} \end{aligned} \quad (4.43)$$

# p-p Scattering

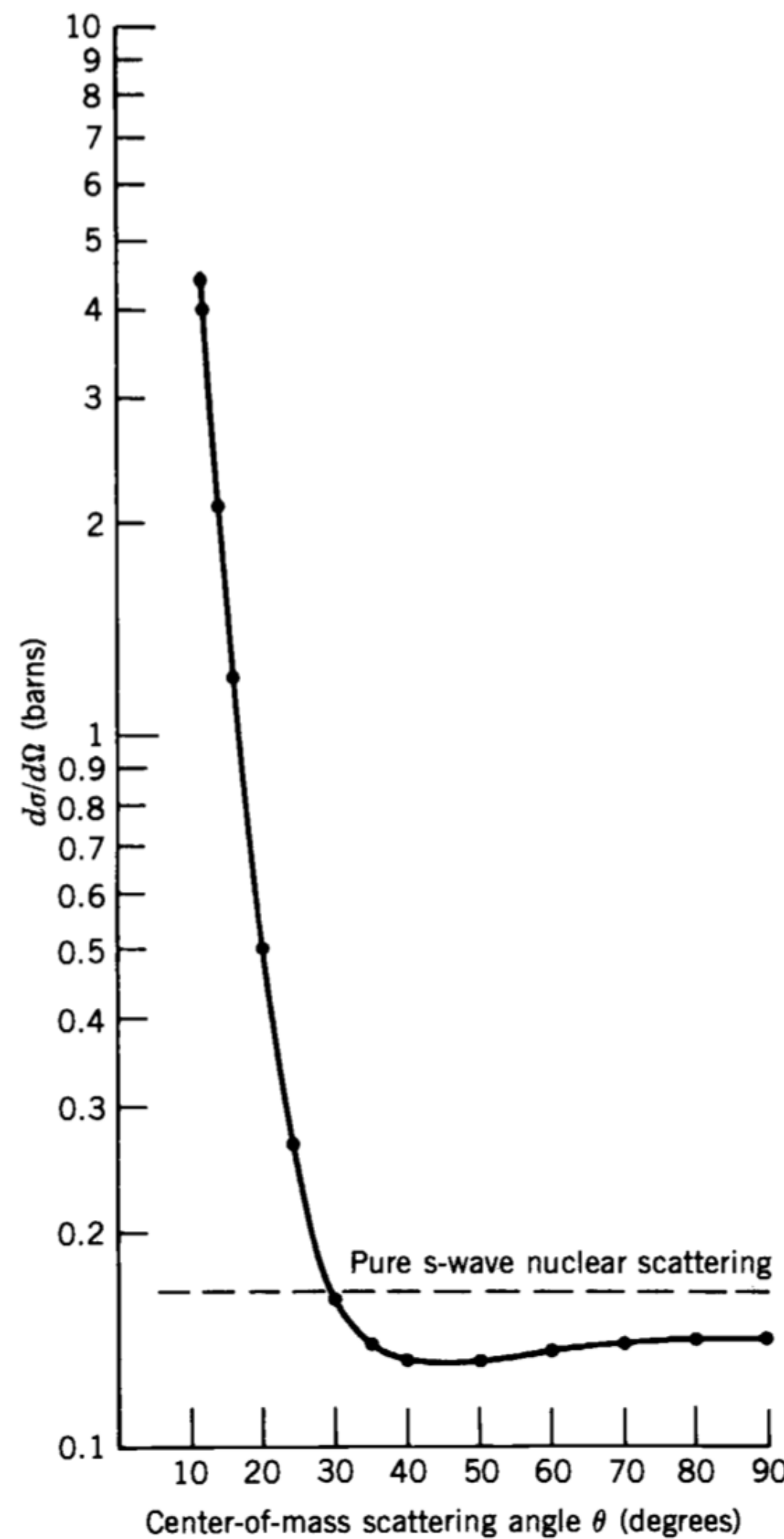


**Figure 4.9** The cross section for low-energy proton–proton scattering at an incident proton energy of 3.037 MeV. Fitting the data points to Equation 4.43 gives the s-wave phase shift  $\delta_0 = 50.966^\circ$ . The cross section for pure nuclear scattering would be 0.165 b; the observation of values of the cross section *smaller* than the pure nuclear value is evidence of the interference between the Coulomb and nuclear parts of the wave function. Data from D. J. Knecht et al., *Phys. Rev.* **148**, 1031 (1966).

# p-p Scattering

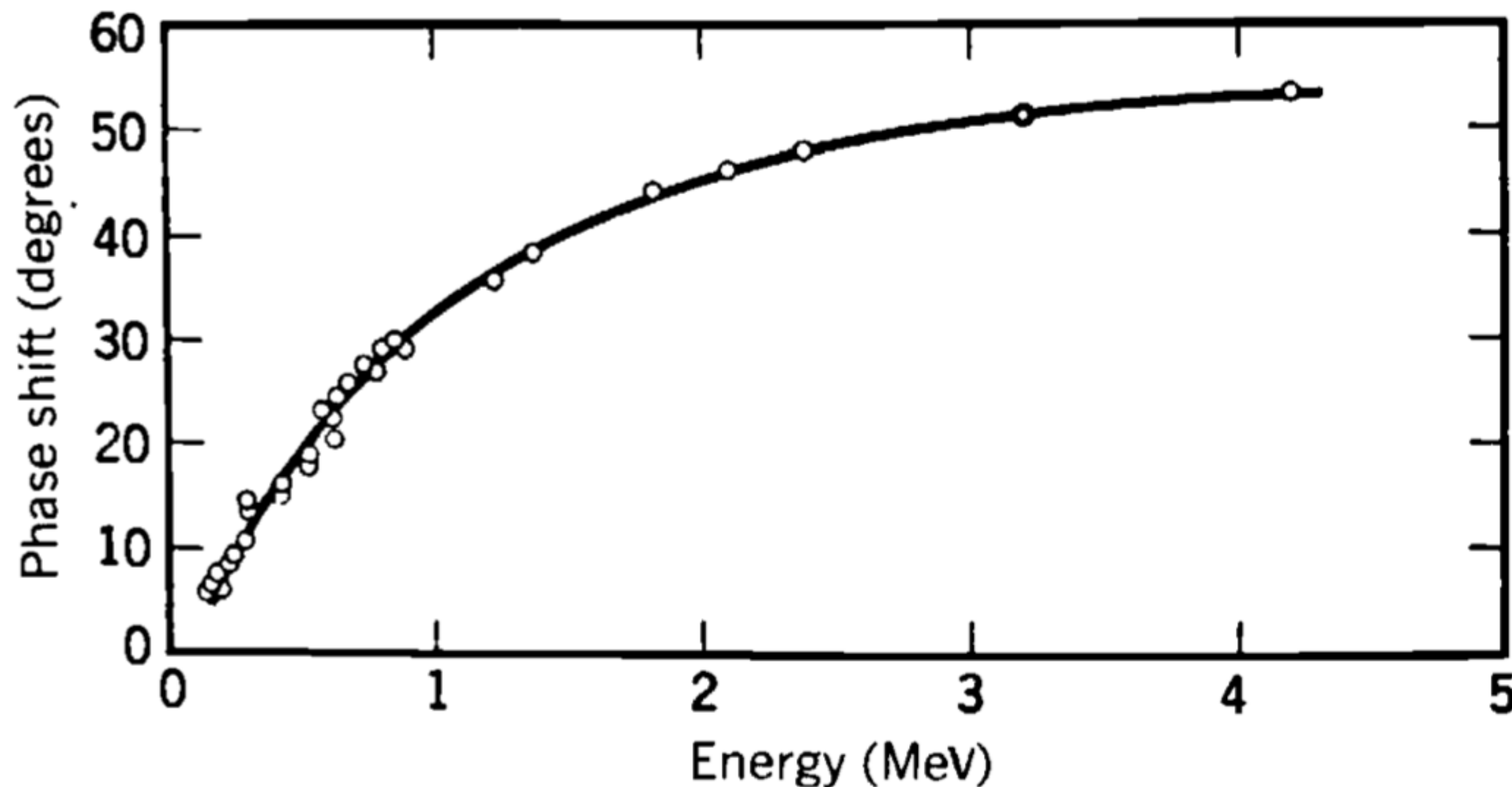


**Figure 4.10** The s-wave phase shift for pp scattering as deduced from the experimental results of several workers.

# Near charge independence

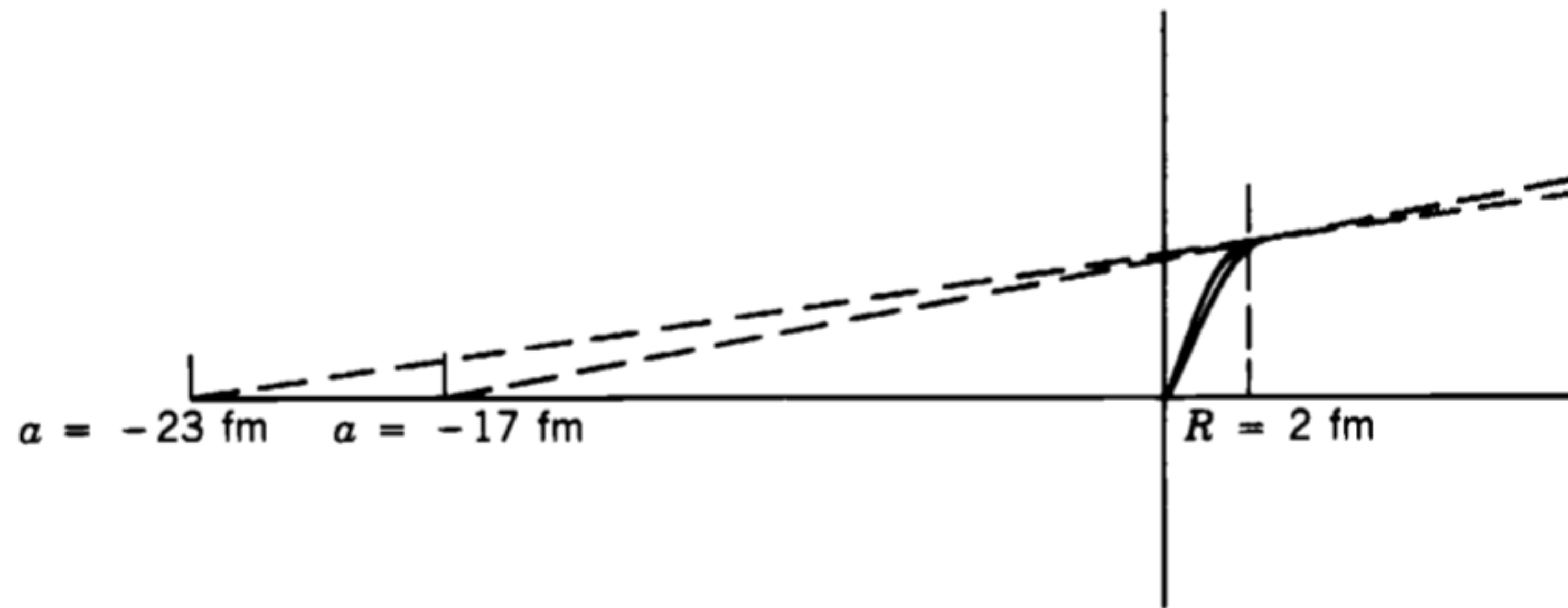


**Figure 4.11** Very small changes in the nucleon–nucleon wave function near  $r = R$  can lead to substantial differences in the scattering length when the extrapolation is made (compare Figure 4.7b).

# Repulsive potential at short distances

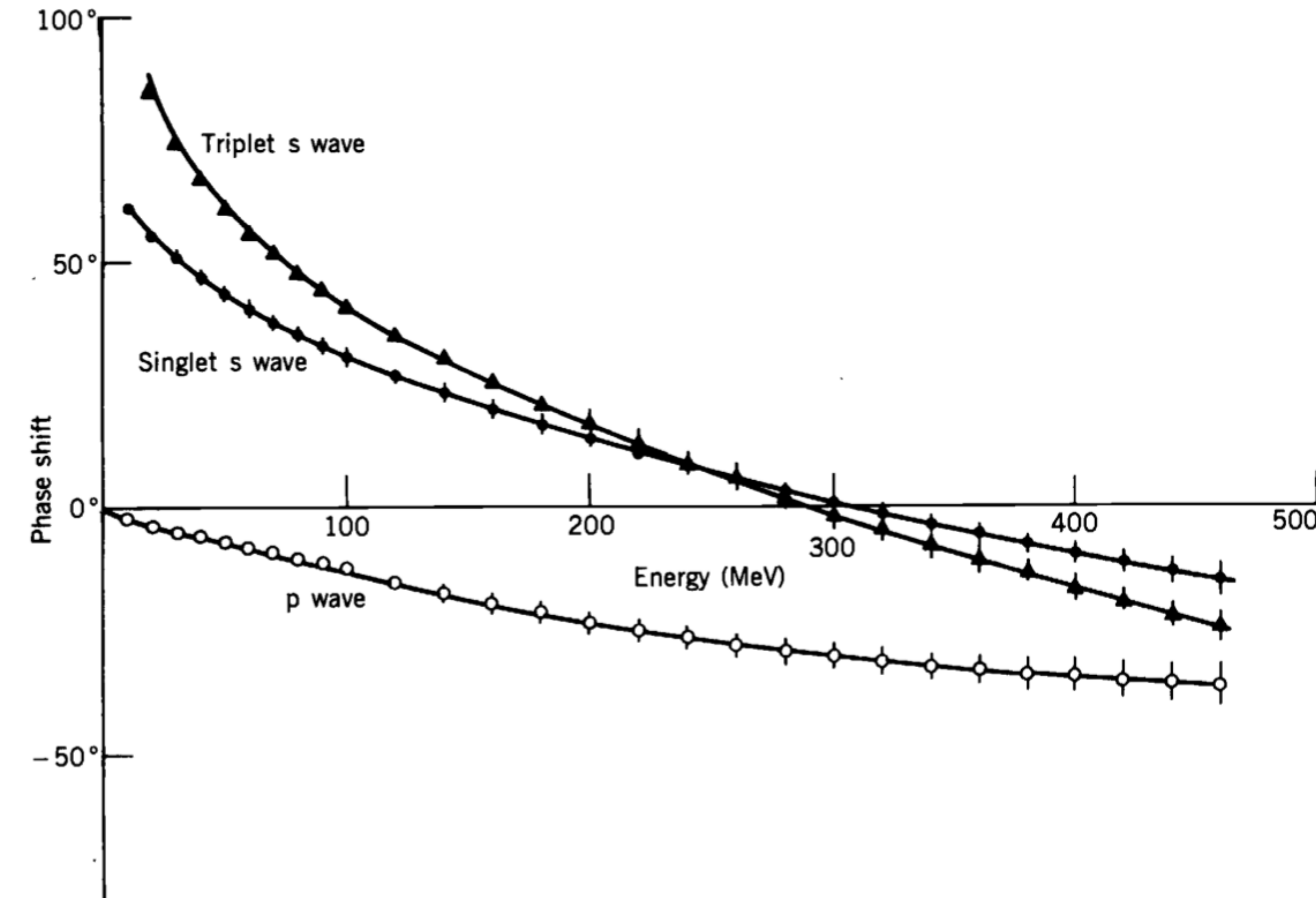


**Figure 4.12** The phase shifts from neutron–proton scattering at medium energies. The change in the s-wave phase shift from positive to negative at about 300 MeV shows that at these energies the incident nucleon is probing a repulsive core in the nucleon–nucleon interaction. ▲,  $^3S_1$ ; ●,  $^1S_0$ ; ○,  $^1P_1$ . Data from M. MacGregor et al., *Phys. Rev.* **182**, 1714 (1969).

# Polarisation

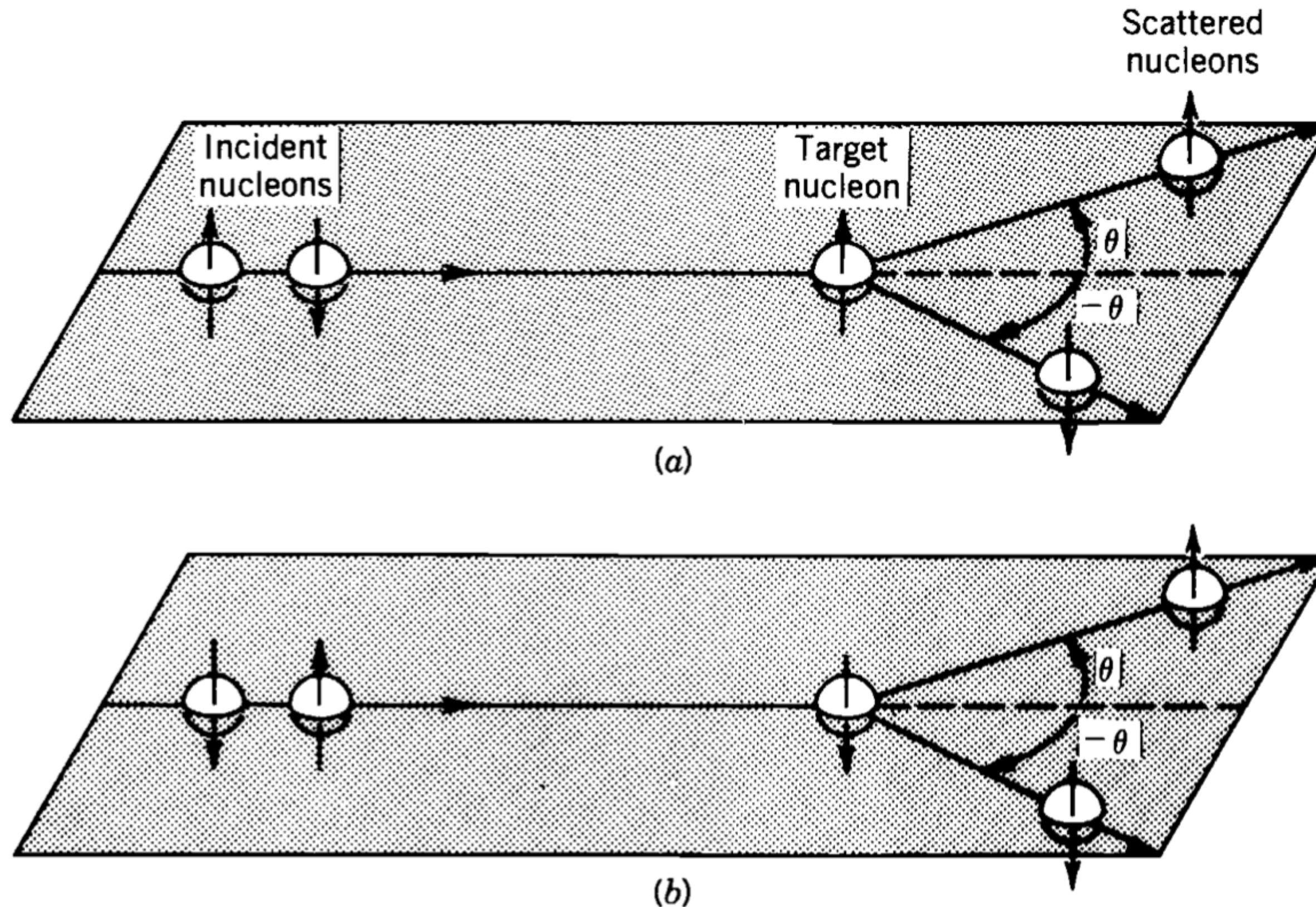


**Figure 4.13** An unpolarized beam (shown as a mixture of spin-up and spin-down nucleons) is scattered from a target that can have either spin up or spin down. In part *a*, the incident nucleons with spin up are scattered to the left at angle  $\theta$ , while those with spin down are scattered to the right at  $-\theta$ . Part *b* can be obtained from part *a* by viewing from below or by rotating  $180^\circ$  about the beam direction; it shows that the same conclusions follow in scattering from a spin-down polarized target.

# Polarisation

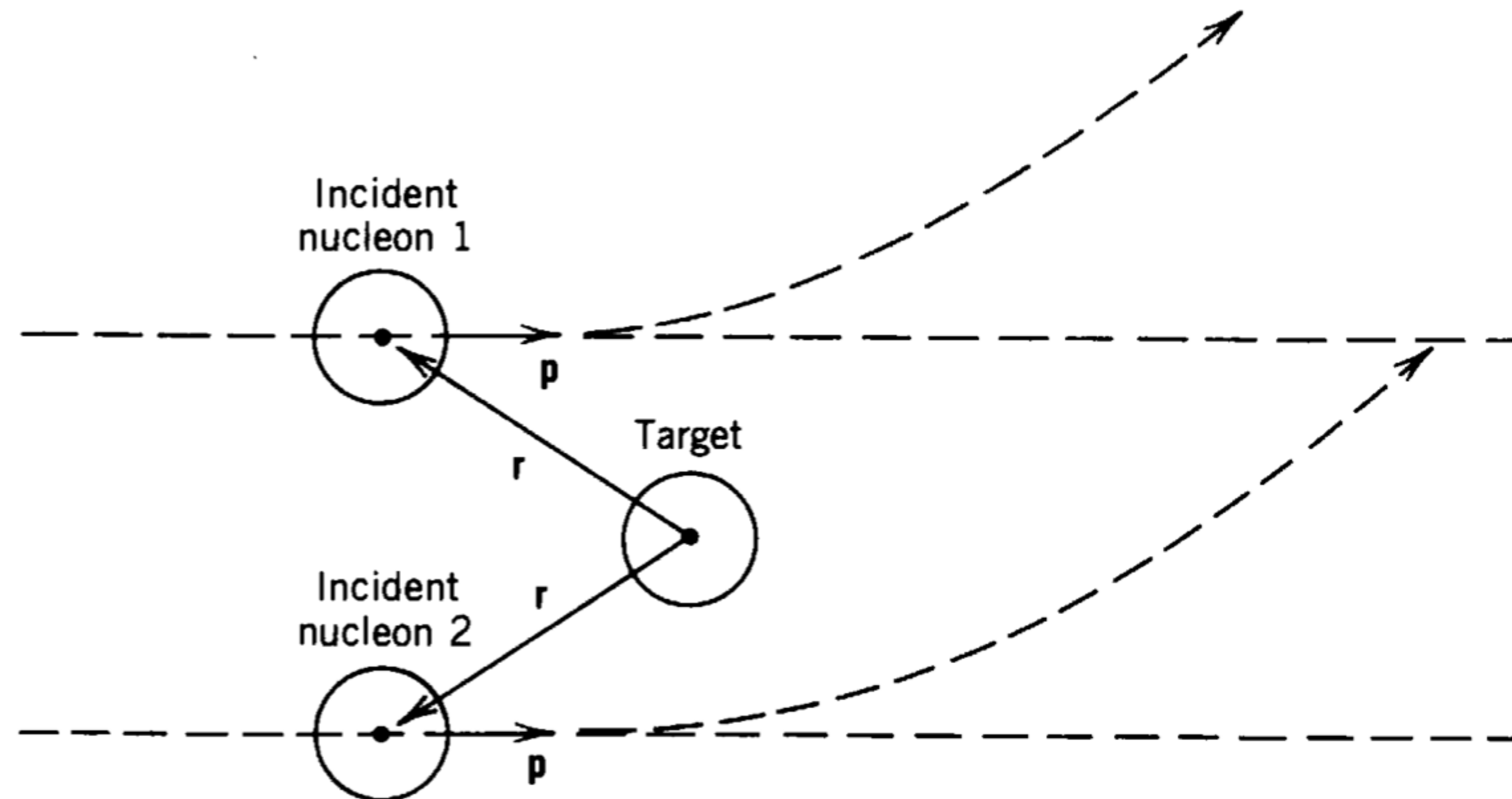


**Figure 4.14** Top view of nucleon–nucleon scattering experiment. All spins point up (out of the paper). Incident nucleon 1 has  $\mathbf{r} \times \mathbf{p}$  into the paper, and thus  $\ell \cdot \mathbf{S}$  is negative, giving a repulsive force and scattering to the left. Incident nucleon 2 has  $\mathbf{r} \times \mathbf{p}$  out of the paper, resulting in an attractive force and again scattering to the left.

# Polarisation

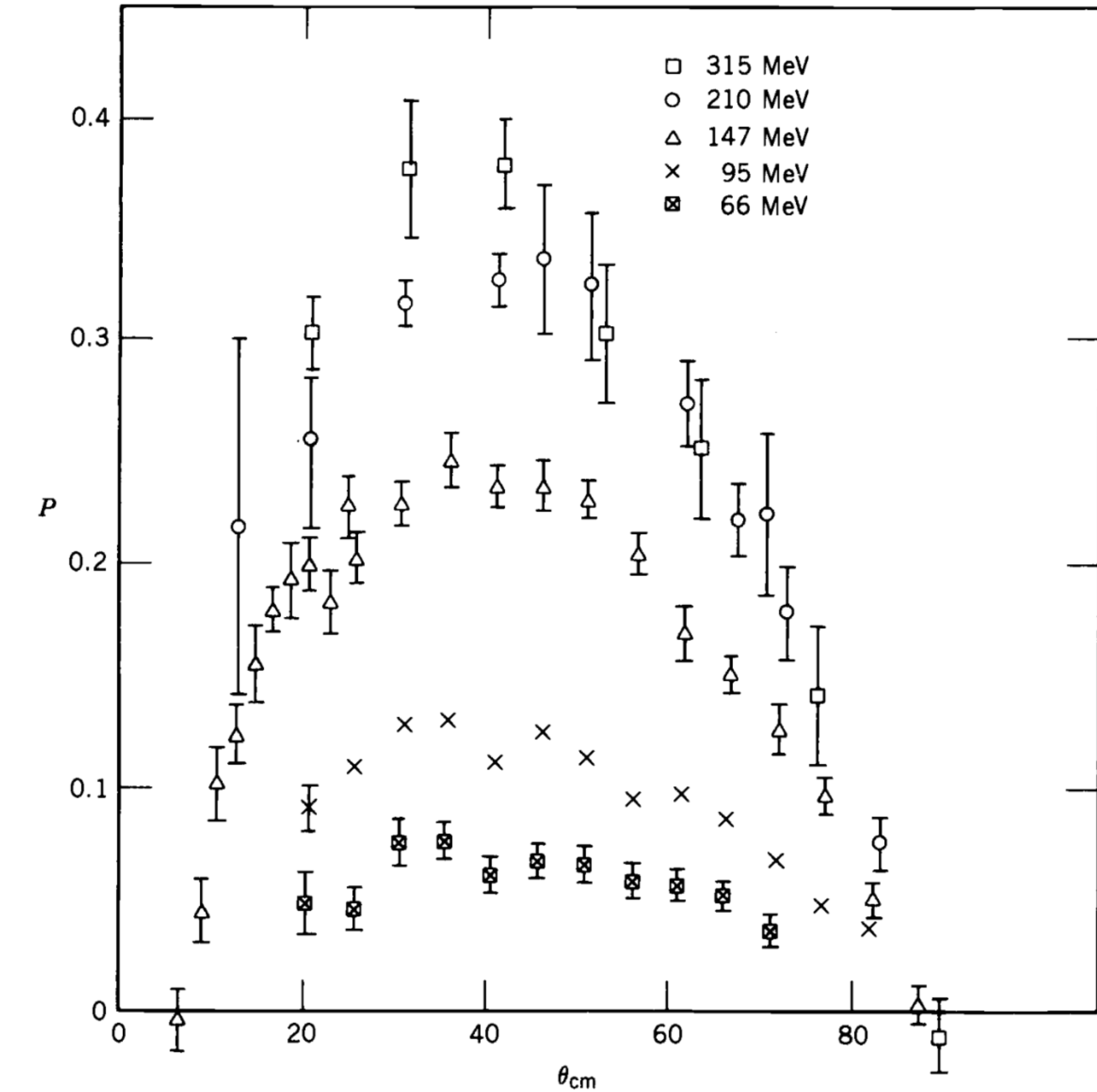


**Figure 4.15** As the incident energy in proton–proton scattering increases, the maximum polarization increases. From R. Wilson, *The Nucleon–Nucleon Interaction* (New York: Wiley-Interscience, 1963).

# The exchange force

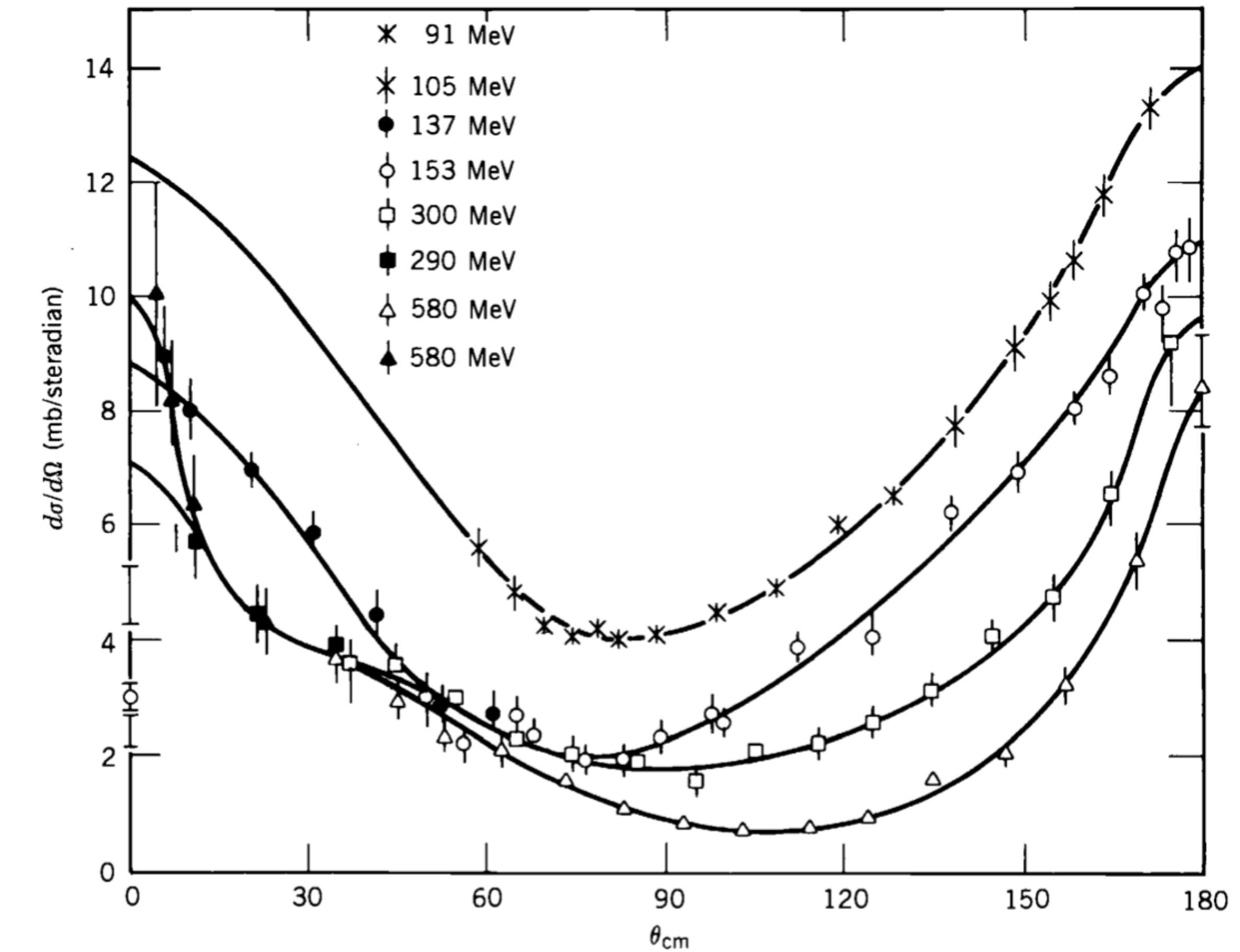
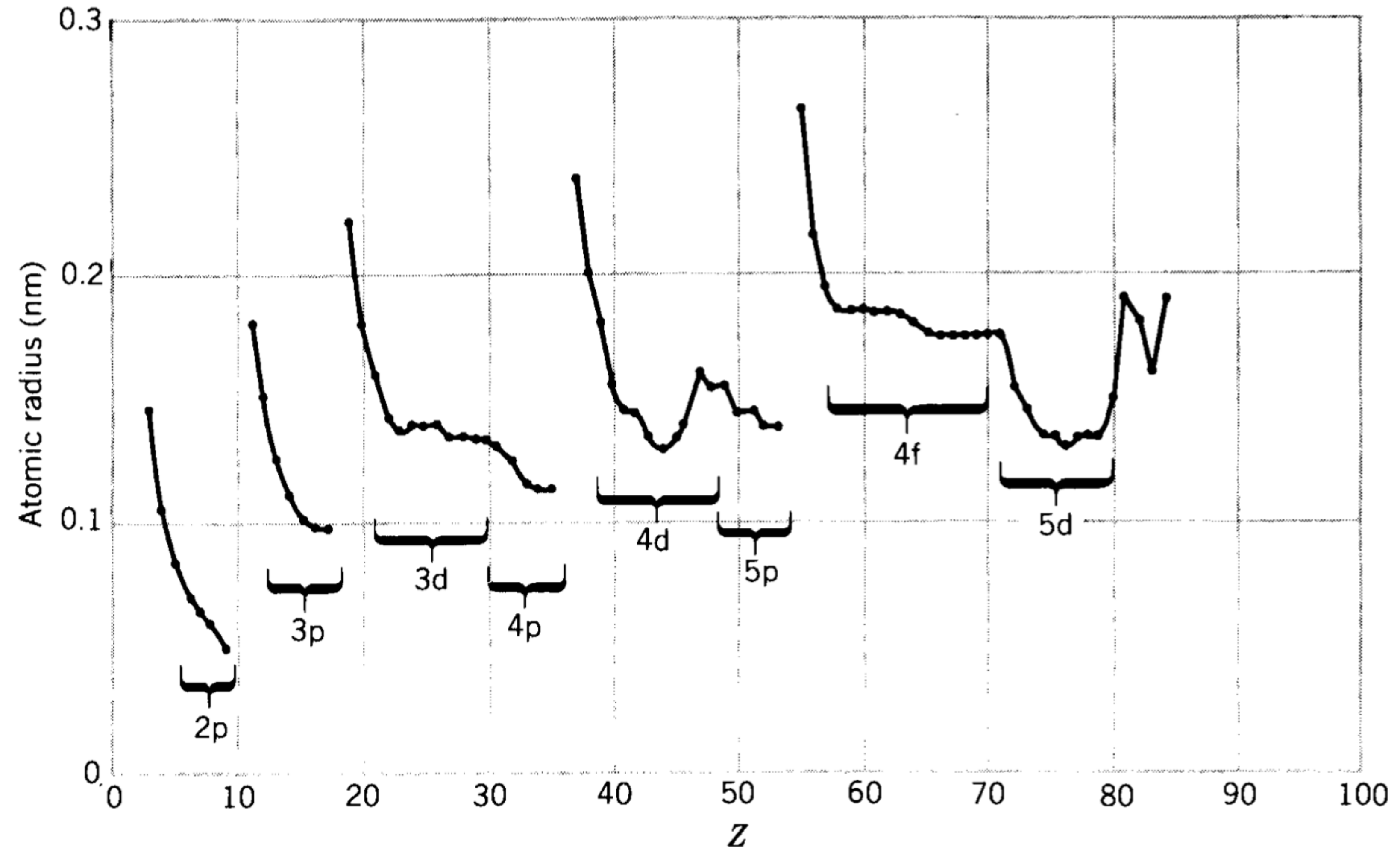


**Figure 4.17** The neutron–proton differential cross section at medium energies. The strong forward-scattering peak (near  $0^\circ$ ) is expected; the equally strong backward peak (near  $180^\circ$ ) is evidence for the exchange force. From R. Wilson, *The Nucleon–Nucleon Interaction* (New York: Wiley-Interscience, 1963).

# Atomic shells



# atomic shells

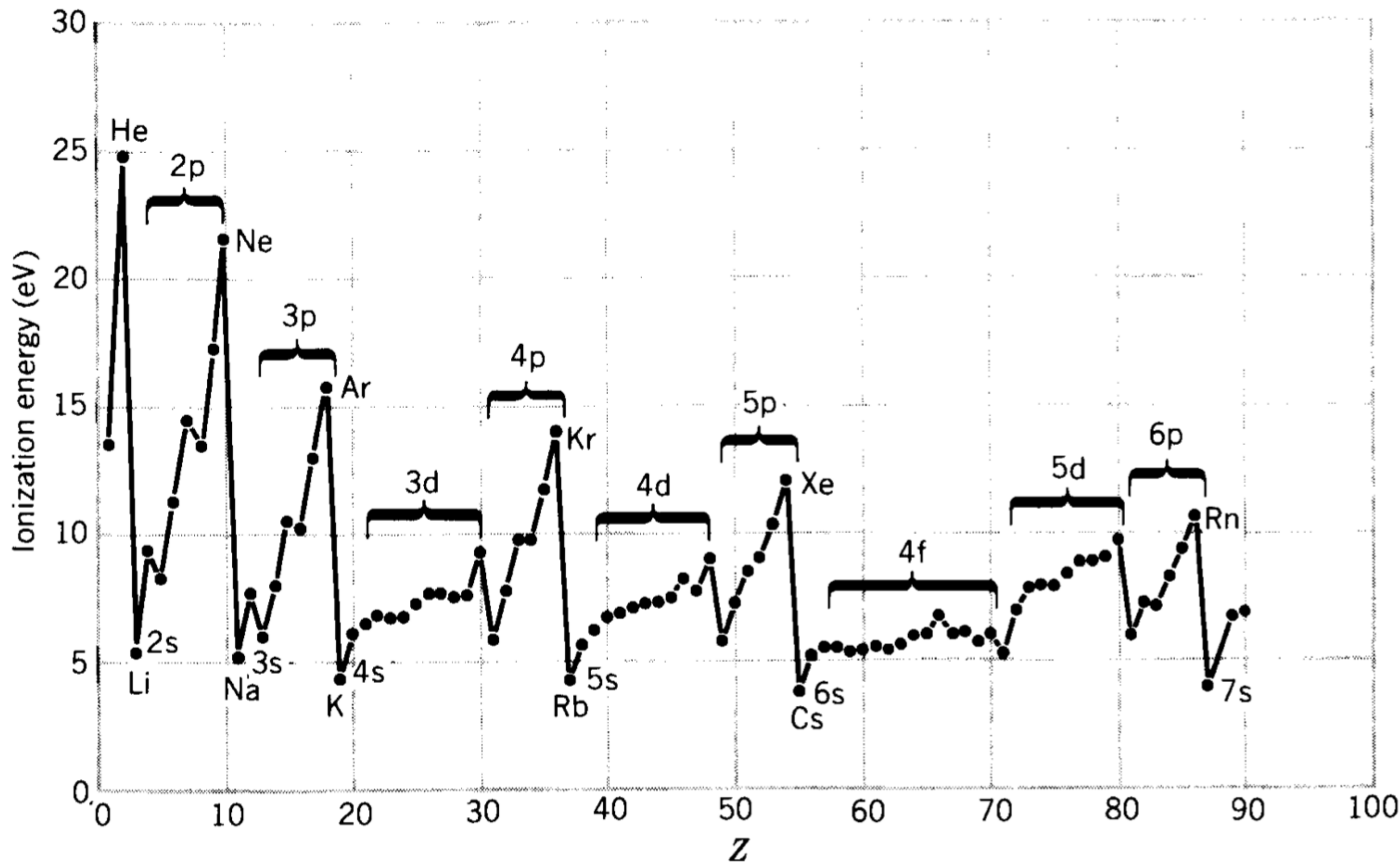


**Figure 5.1** Atomic radius (top) and ionization energy (bottom) of the elements. The smooth variations in these properties correspond to the gradual filling of an atomic shell, and the sudden jumps show transitions to the next shell.

# Shell model

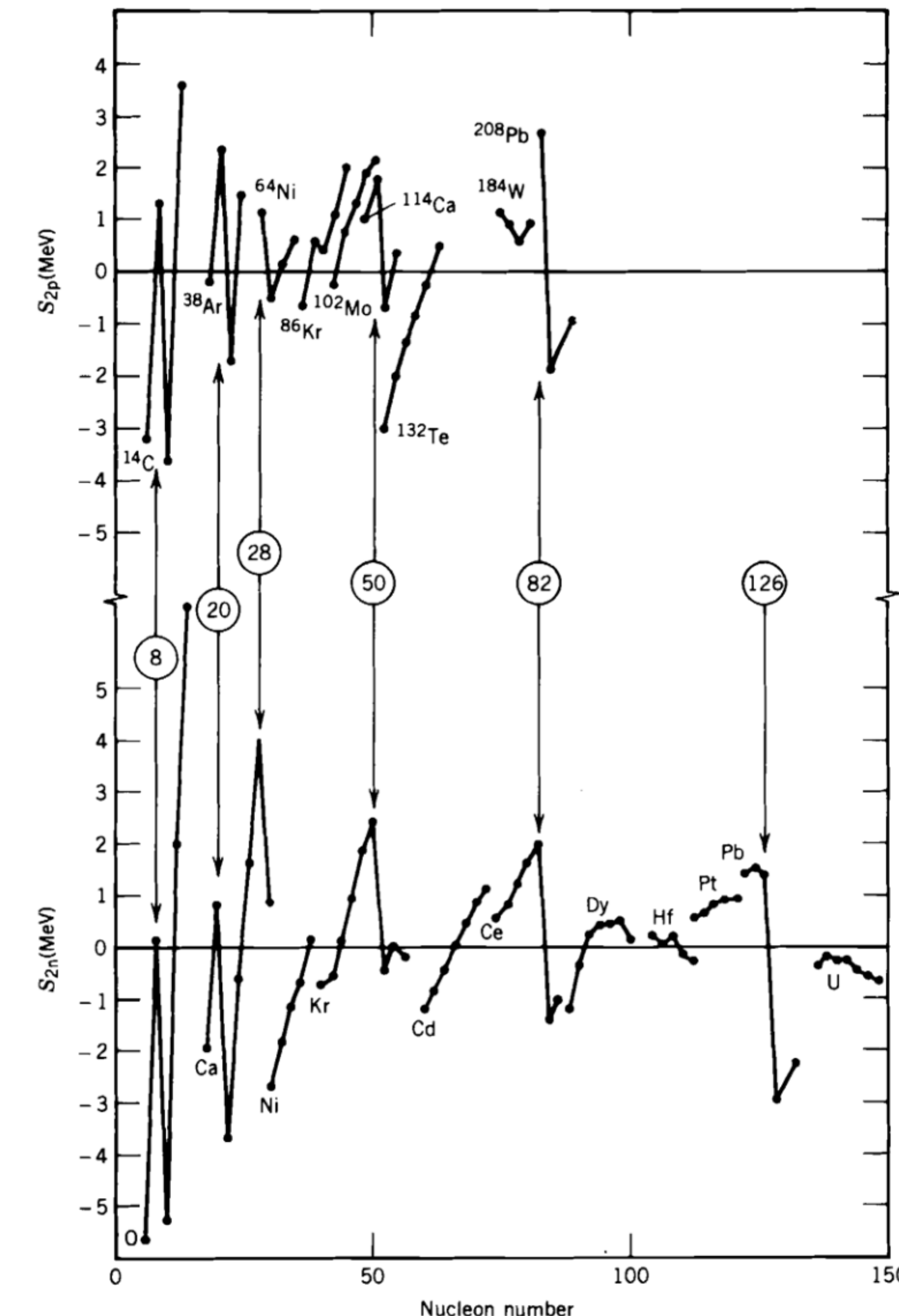


**Figure 5.2** (Top) Two-proton separation energies of sequences of isotones (constant  $N$ ). The lowest  $Z$  member of each sequence is noted. (Bottom) Two-neutron separation energies of sequences of isotopes. The sudden changes at the indicated “magic numbers” are apparent. The data plotted are differences between the measured values and the predictions of the semiempirical mass formula. Measured values are from the 1977 atomic mass tables (A. H. Wapstra and K. Bos, *Atomic Data and Nuclear Data Tables* **19**, 215 (1977)).

# Shell model

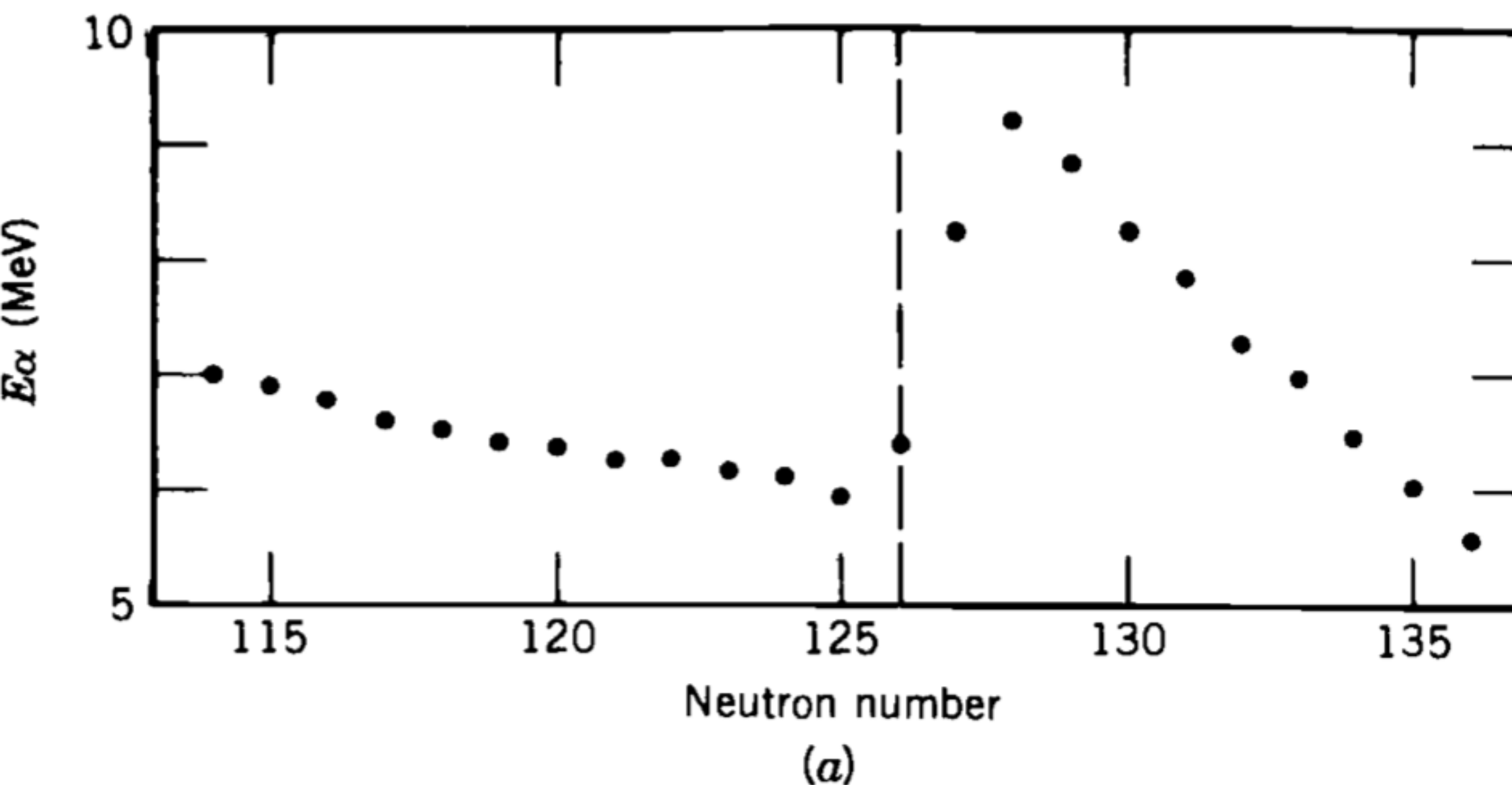
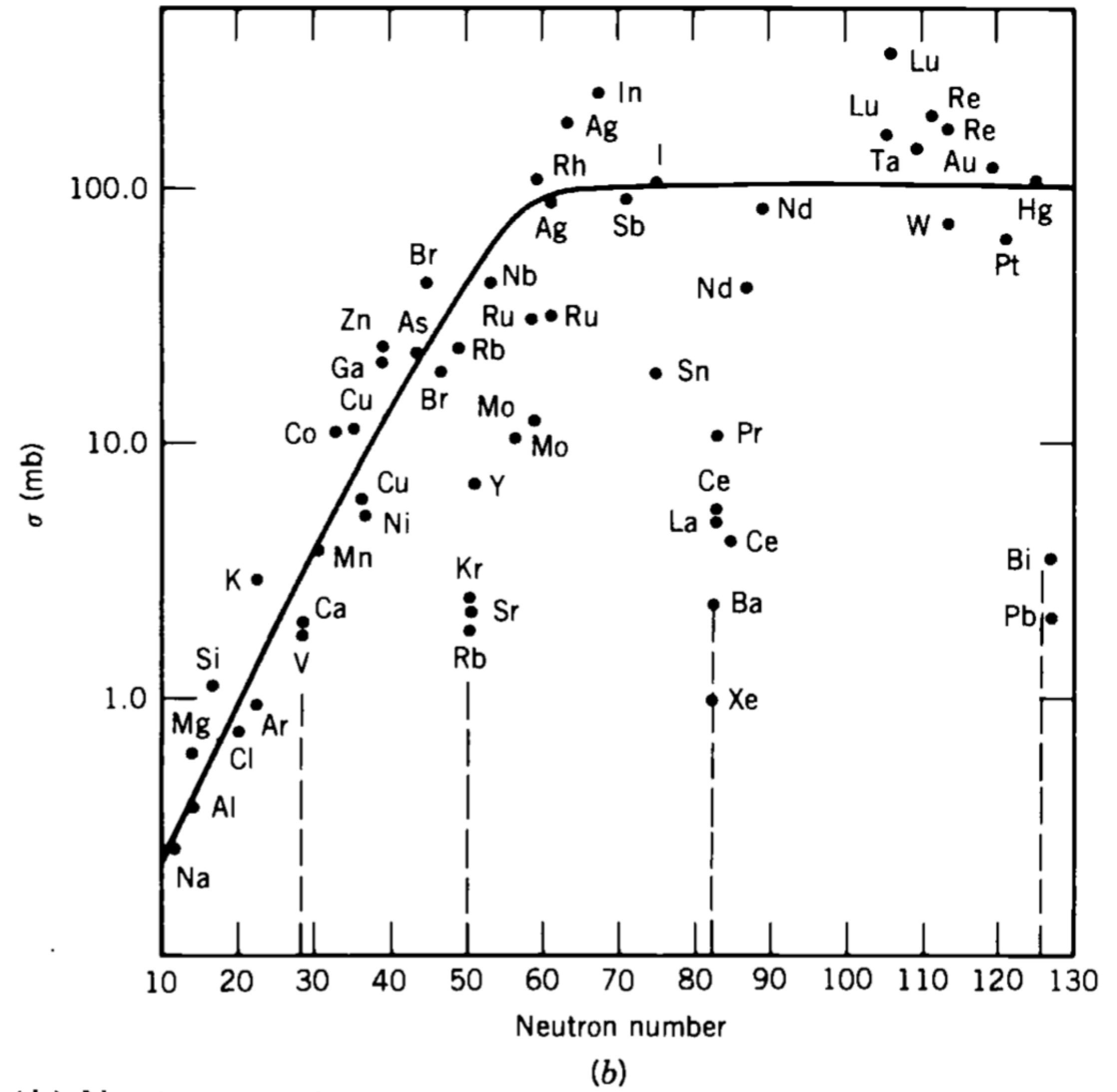


**Figure 5.3** Additional evidence for nuclear shell structure. (a) Energies of  $\alpha$  particles emitted by isotopes of Rn. Note the sudden increase when the *daughter* has  $N = 126$  (i.e., when the parent has  $N = 128$ ). If the daughter nucleus is more tightly bound, the  $\alpha$  decay is able to carry away more energy. (b) Neutron-capture

# Shell model



tightly bound, the  $\alpha$  decay is able to carry away more energy. (b) Neutron-capture cross sections of various nuclei. Note the decreases by roughly two orders of magnitude near  $N = 50, 82$ , and  $126$ . (c) Change in the nuclear charge radius when

# Shell model

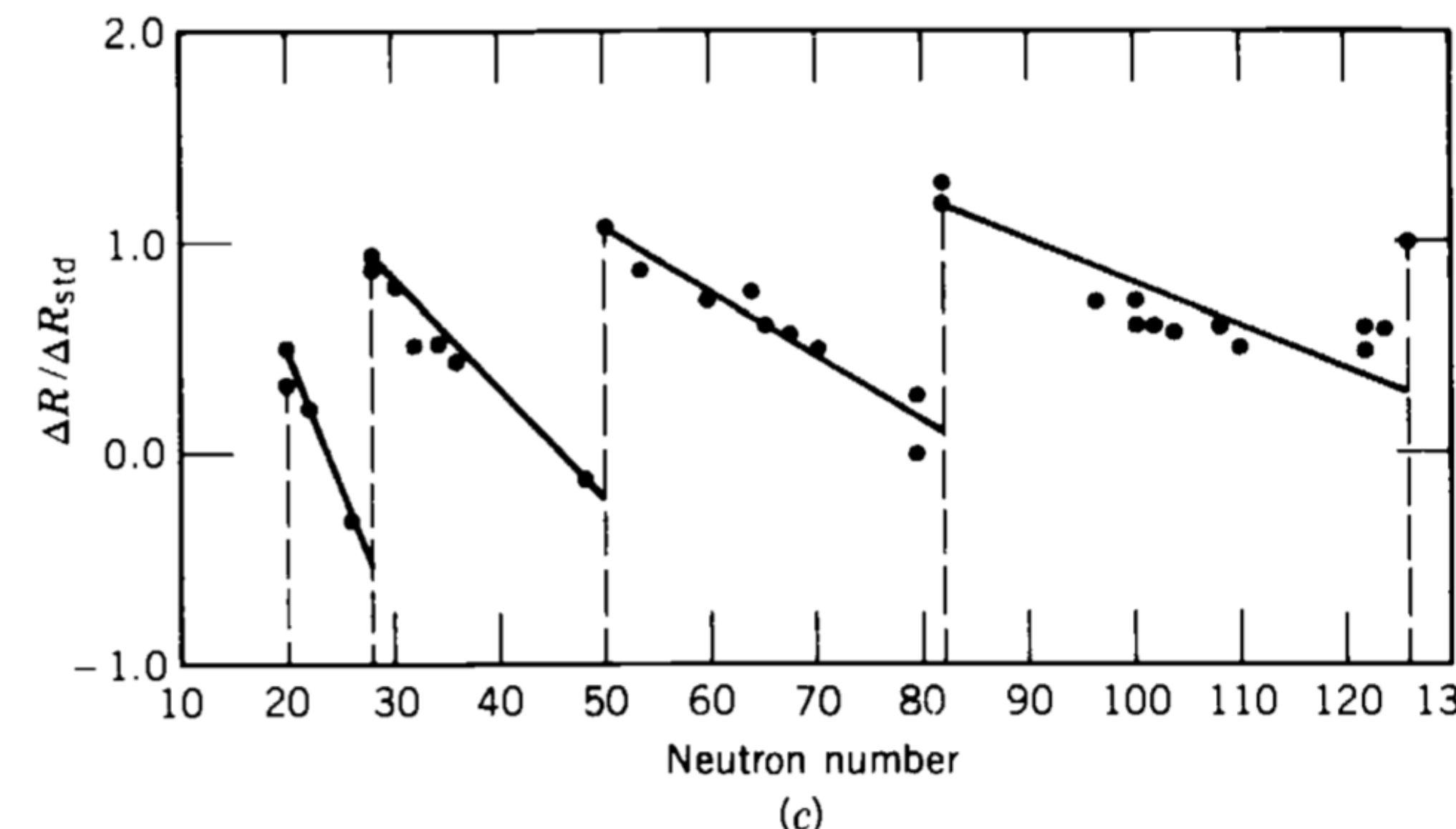


**Figure 5.3** Additional evidence for nuclear shell structure. (a) Energies of  $\alpha$  particles emitted by isotopes of Rn. Note the sudden increase when the *daughter* has  $N = 126$  (i.e., when the parent has  $N = 128$ ). If the daughter nucleus is more tightly bound, the  $\alpha$  decay is able to carry away more energy. (b) Neutron-capture cross sections of various nuclei. Note the decreases by roughly two orders of magnitude near  $N = 50, 82$ , and  $126$ . (c) Change in the nuclear charge radius when  $\Delta N = 2$ . Note the sudden jumps at  $20, 28, 50, 82$ , and  $126$  and compare with Figure 5.1. To emphasize the shell effects, the radius difference  $\Delta R$  has been divided by the standard  $\Delta R$  expected from the  $A^{1/3}$  dependence. From E. B. Shera et al., *Phys. Rev. C* **14**, 731 (1976).

# Shell model

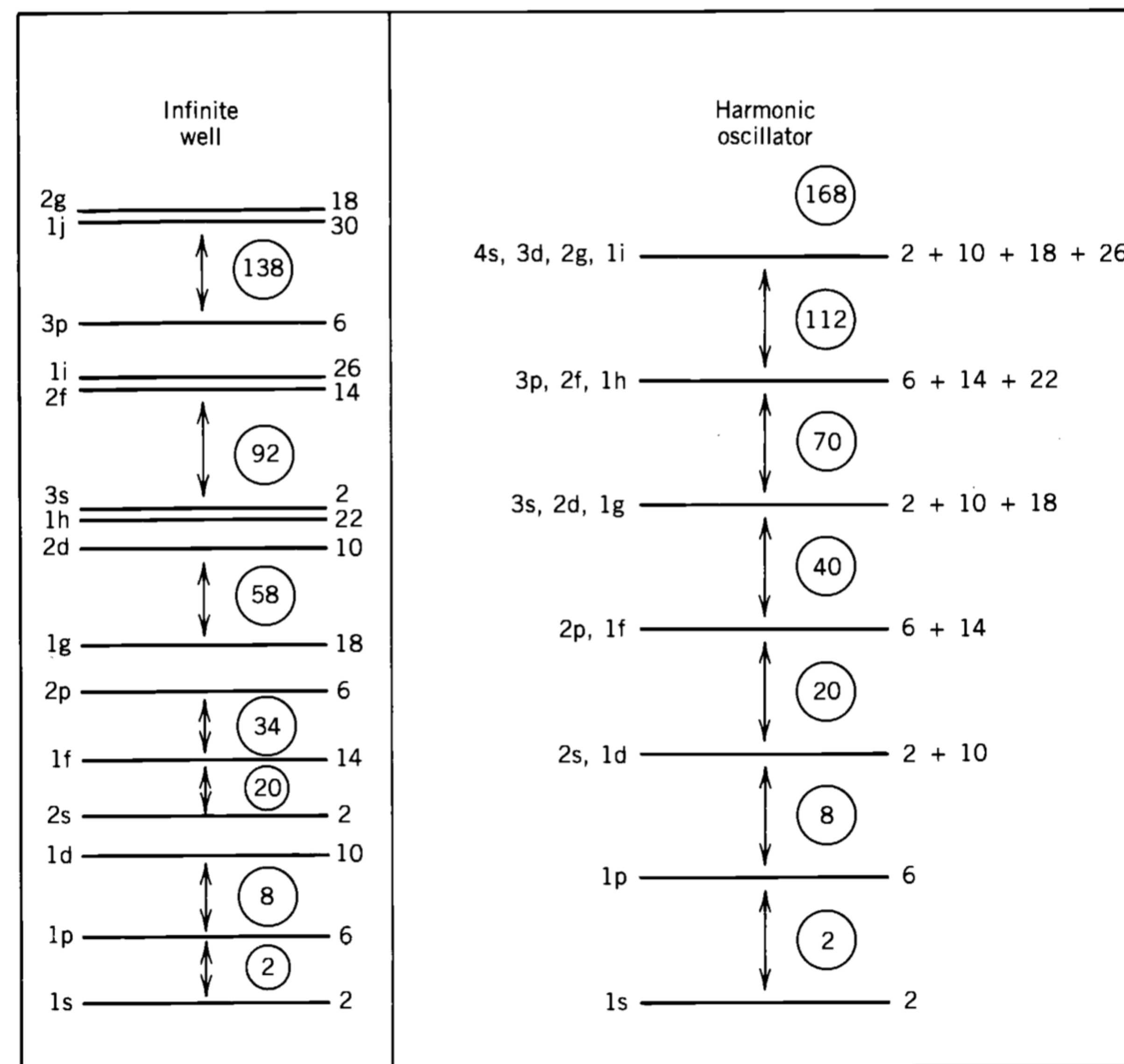


**Figure 5.4** Shell structure obtained with infinite well and harmonic oscillator potentials. The capacity of each level is indicated to its right. Large gaps occur between the levels, which we associate with closed shells. The circled numbers indicate the total number of nucleons at each shell closure.

# Potential

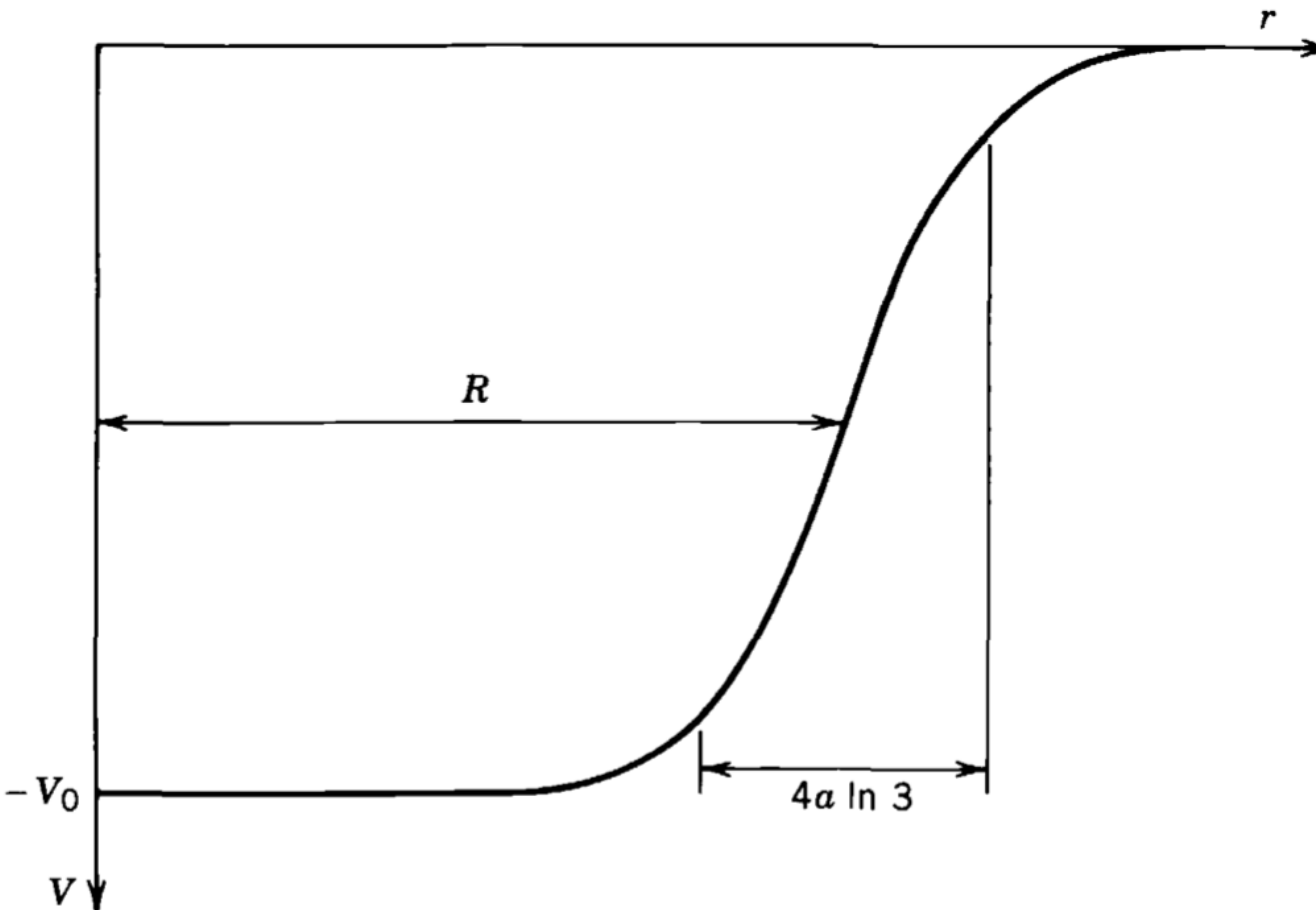


**Figure 5.5** A realistic form for the shell-model potential. The “skin thickness”  $4a \ln 3$  is the distance over which the potential changes from  $0.9V_0$  to  $0.1V_0$ .

# Shell model

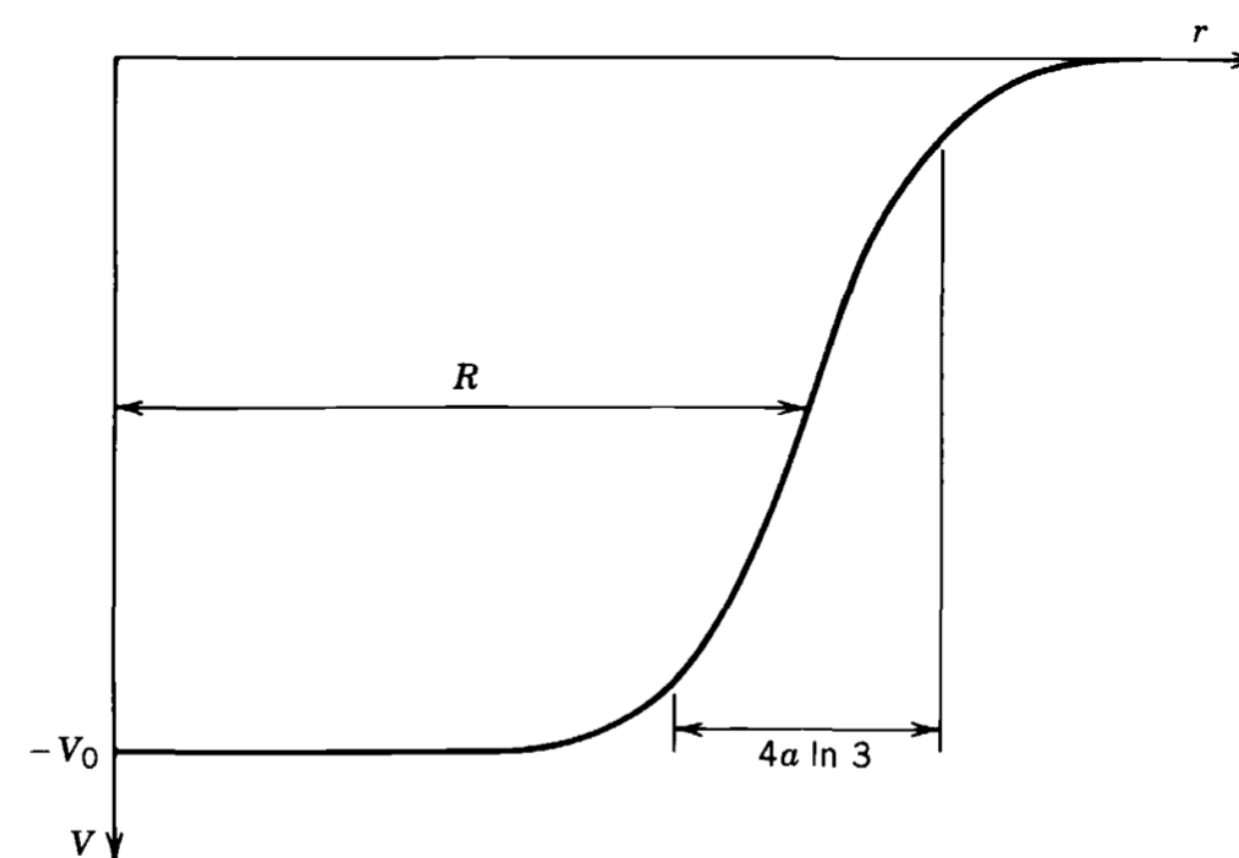


**Figure 5.5** A realistic form for the shell-model potential. The “skin thickness”  $4a \ln 3$  is the distance over which the potential changes from  $0.9V_0$  to  $0.1V_0$ .

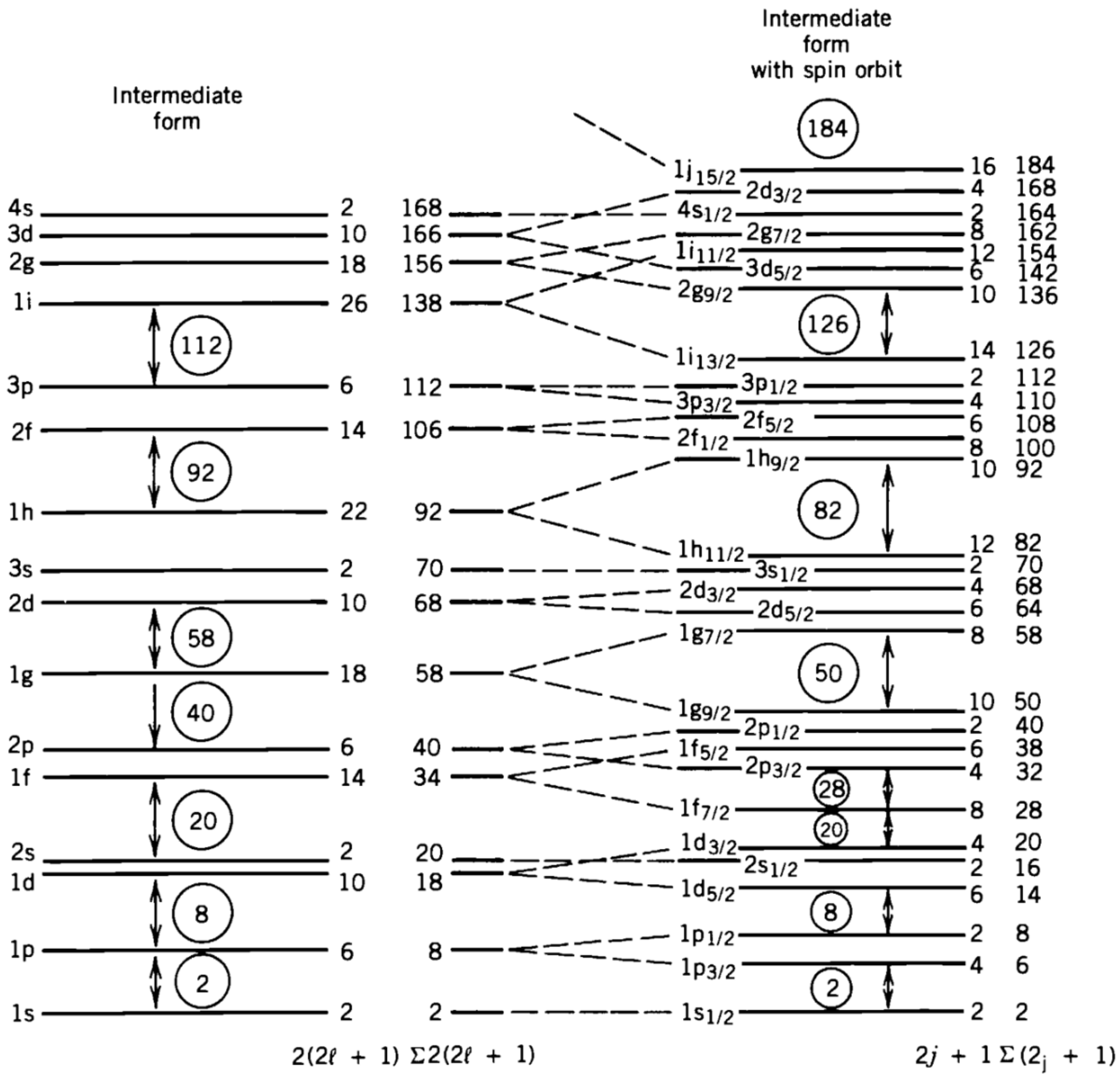


**Figure 5.6** At the left are the energy levels calculated with the potential of Figure 5.5. To the right of each level are shown its capacity and the cumulative number of nucleons up to that level. The right side of the figure shows the effect of the spin-orbit interaction, which splits the levels with  $\ell > 0$  into two new levels. The shell effect is quite apparent, and the magic numbers are exactly reproduced.

# Shell model

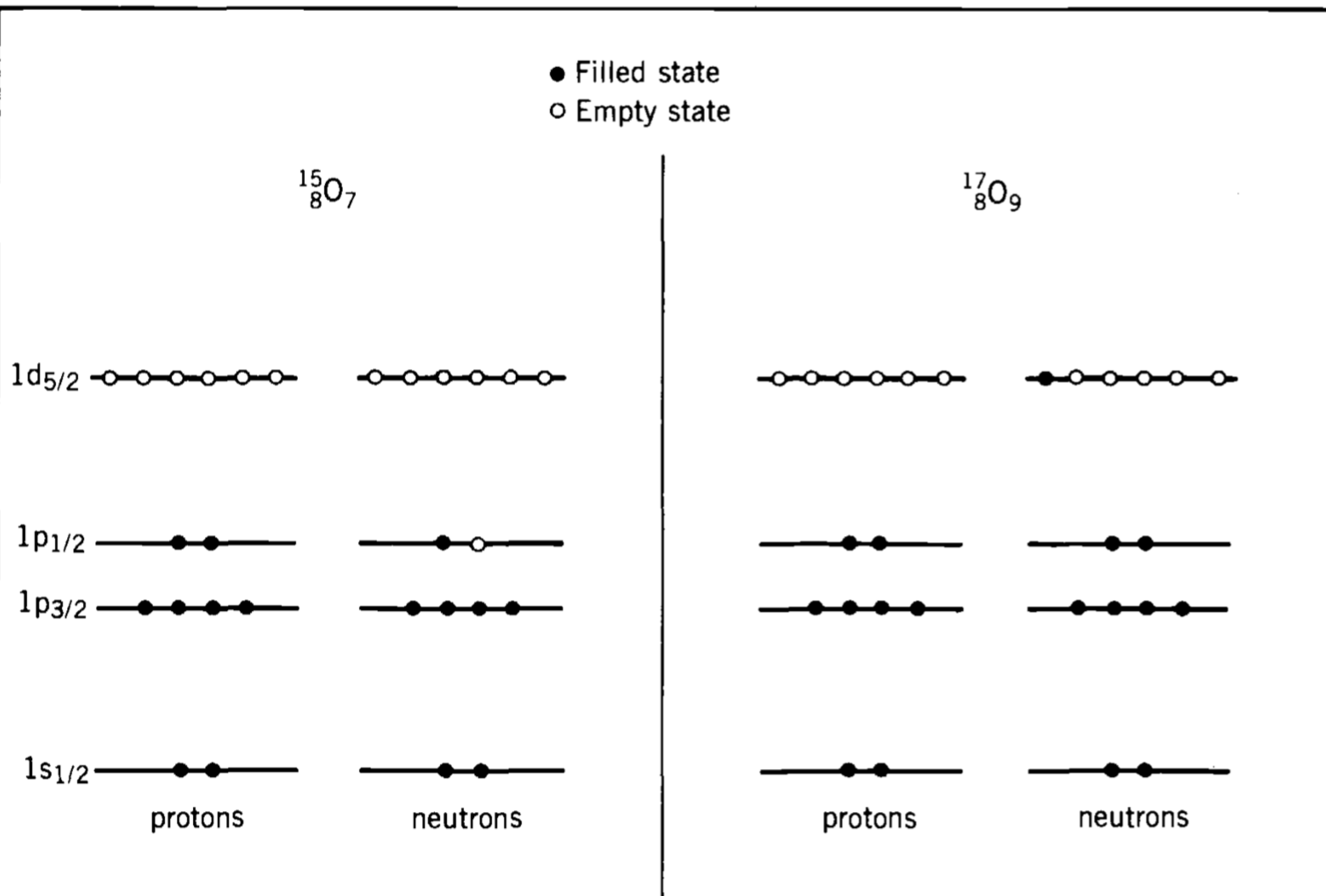


**Figure 5.7** The filling of shells in  $^{15}\text{O}$  and  $^{17}\text{O}$ . The filled proton shells do not contribute to the structure; the properties of the ground state are determined primarily by the odd neutron.

# Shell model

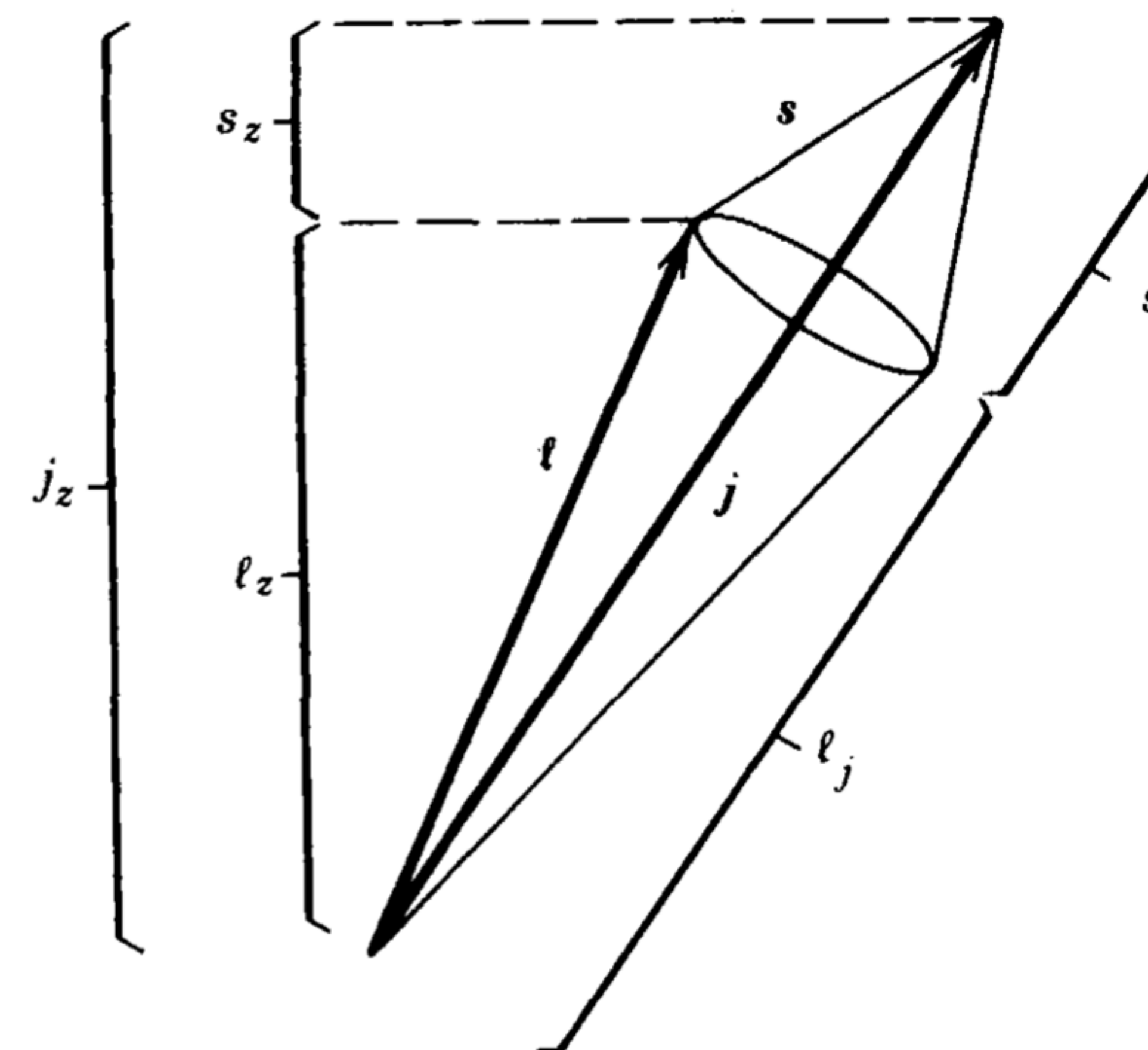


**Figure 5.8** As the total angular momentum  $j$  precesses about the  $z$  axis keeping  $j_z$  constant, the vectors  $\ell$  and  $s$  precess about  $j$ . The components of  $\ell$  and  $s$  along  $j$  remain constant, but  $\ell_z$  and  $s_z$  vary.

# Shell model

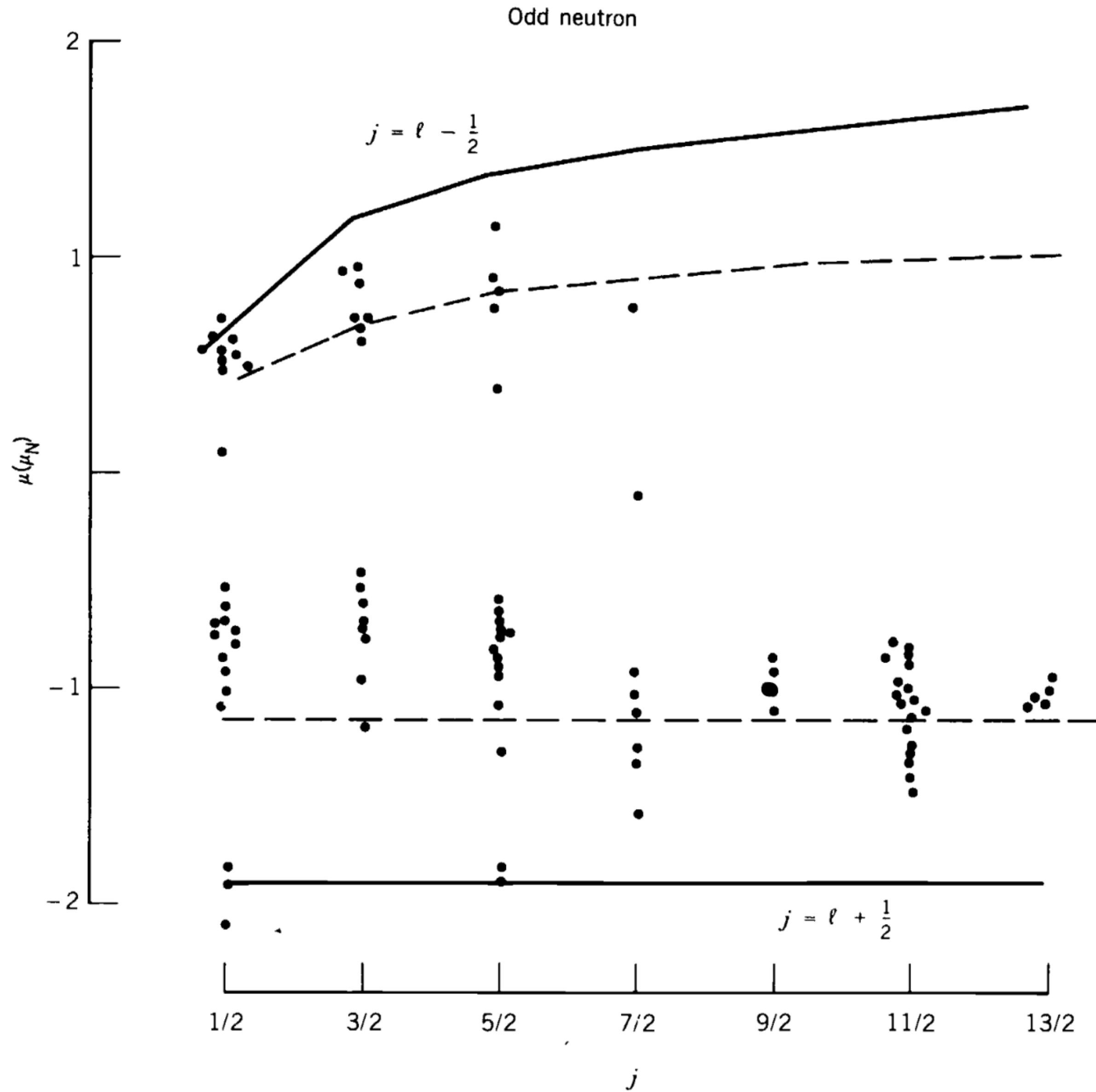


**Figure 5.9** Experimental values for the magnetic moments of odd-neutron and odd-proton shell-model nuclei. The Schmidt lines are shown as solid for  $g_s = g_s(\text{free})$  and dashed for  $g_s = 0.6g_s(\text{free})$ .

# Shell model

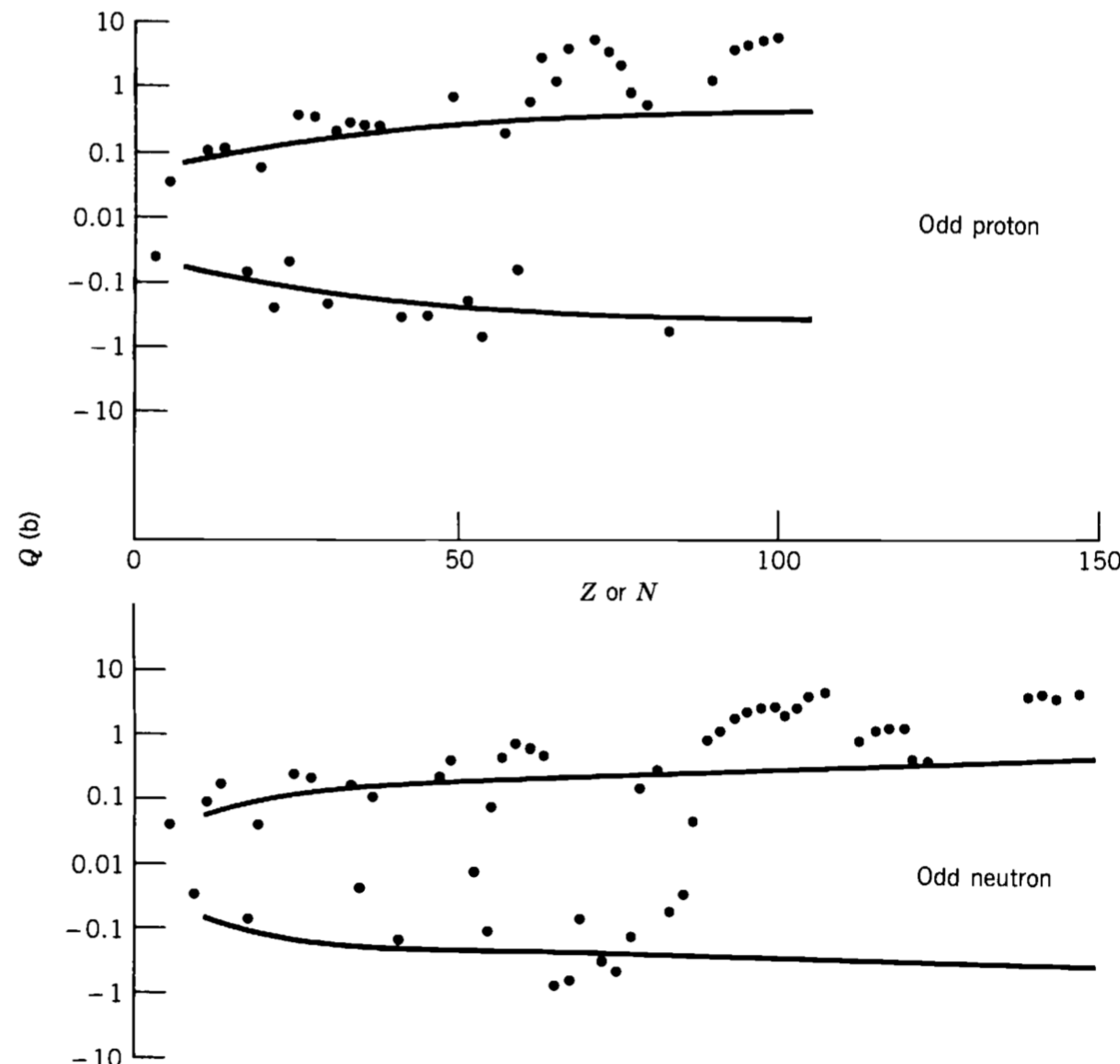


**Figure 5.10** Experimental values of electric quadrupole moments of odd-neutron and odd-proton nuclei. The solid lines show the limits  $Q \sim \langle r^2 \rangle$  expected for shell-model nuclei. The data are within the limits, except for the regions  $60 < Z < 80$ ,  $Z > 90$ ,  $90 < N < 120$ , and  $N > 140$ , where the experimental values are more than an order of magnitude larger than predicted by the shell model.

# Shell model

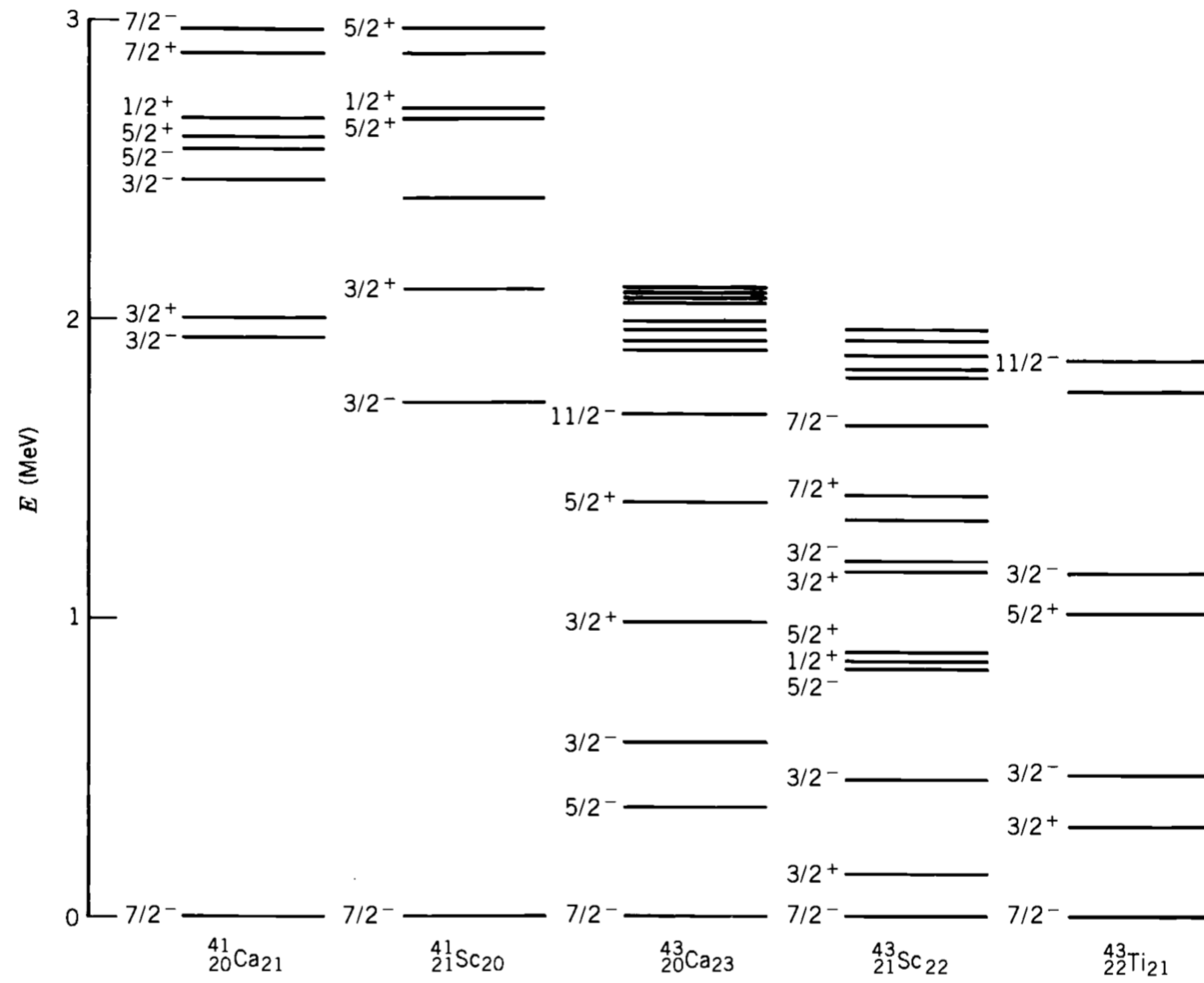


**Figure 5.12** Energy levels of nuclei with odd particles in the  $1f_{7/2}$  shell.

# Liquid drop model

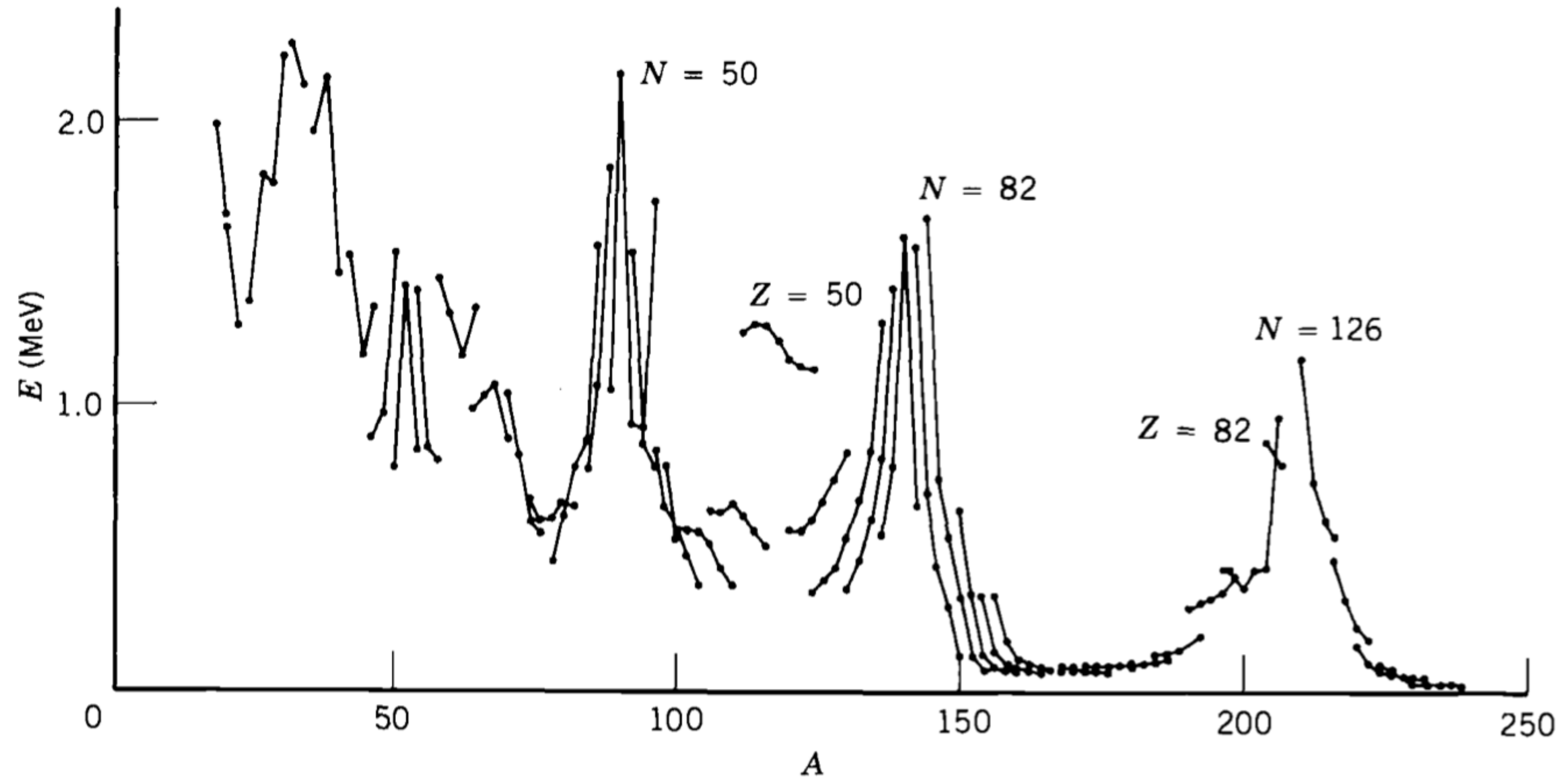


**Figure 5.15a** Energies of lowest  $2^+$  states of even- $Z$ , even- $N$  nuclei. The lines connect sequences of isotopes.

# Liquid drop model

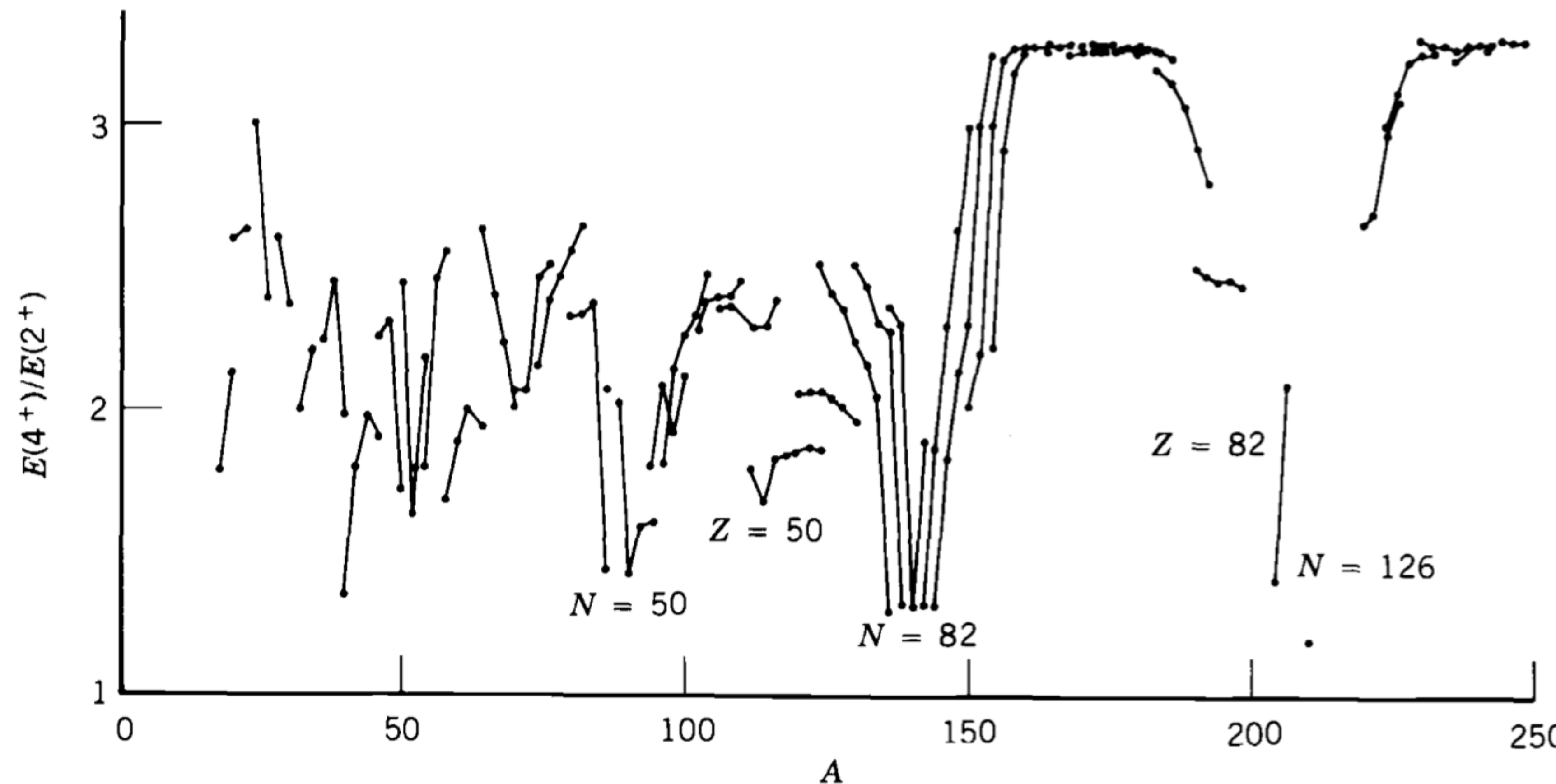


**Figure 5.15b** The ratio  $E(4^+)/E(2^+)$  for the lowest  $2^+$  and  $4^+$  states of even- $Z$ , even- $N$  nuclei. The lines connect sequences of isotopes.

# Liquid drop model

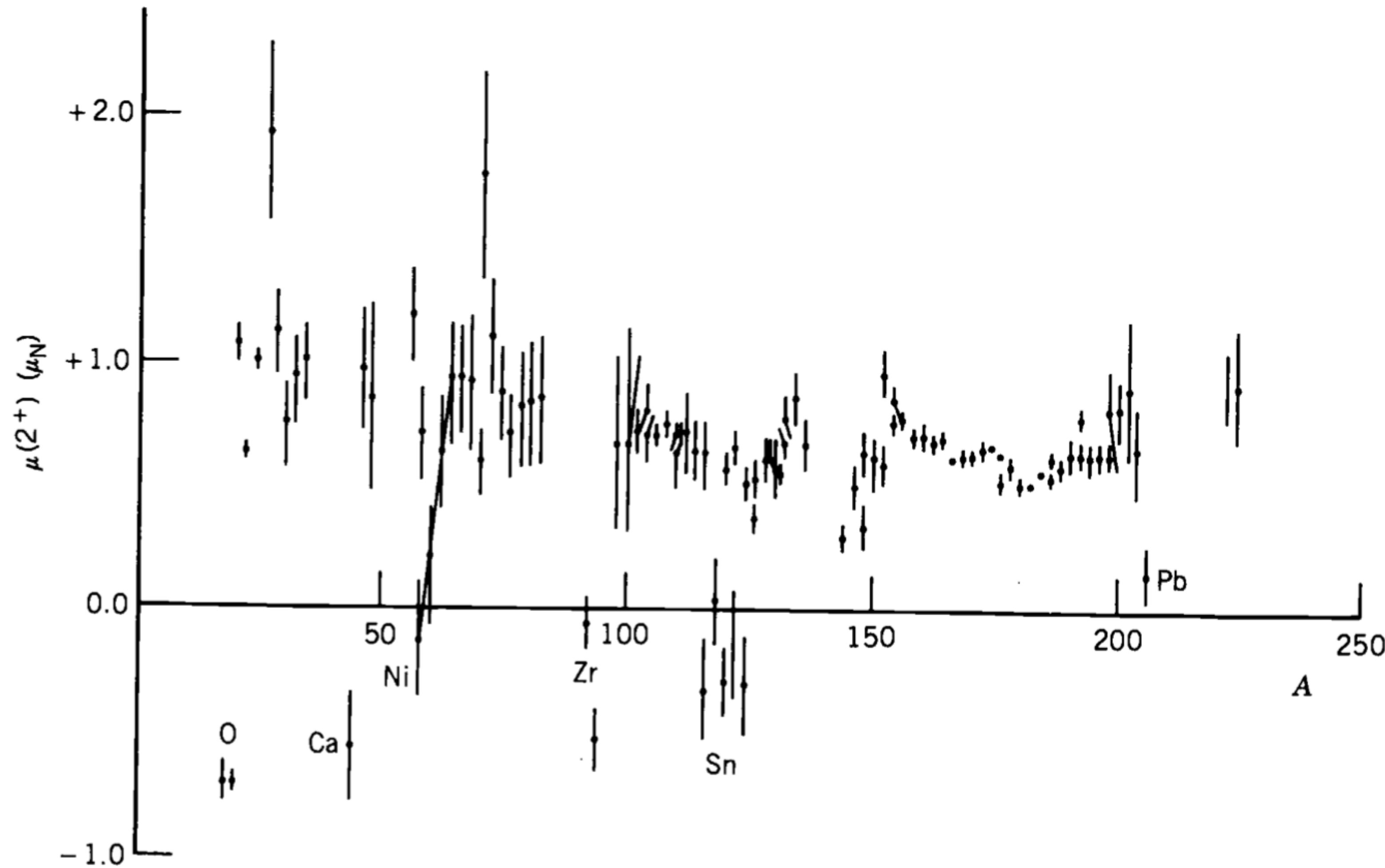


**Figure 5.16a** Magnetic moments of lowest  $2^+$  states of even- $Z$ , even- $N$  nuclei. Shell-model nuclei showing noncollective behavior are indicated.

# Liquid drop

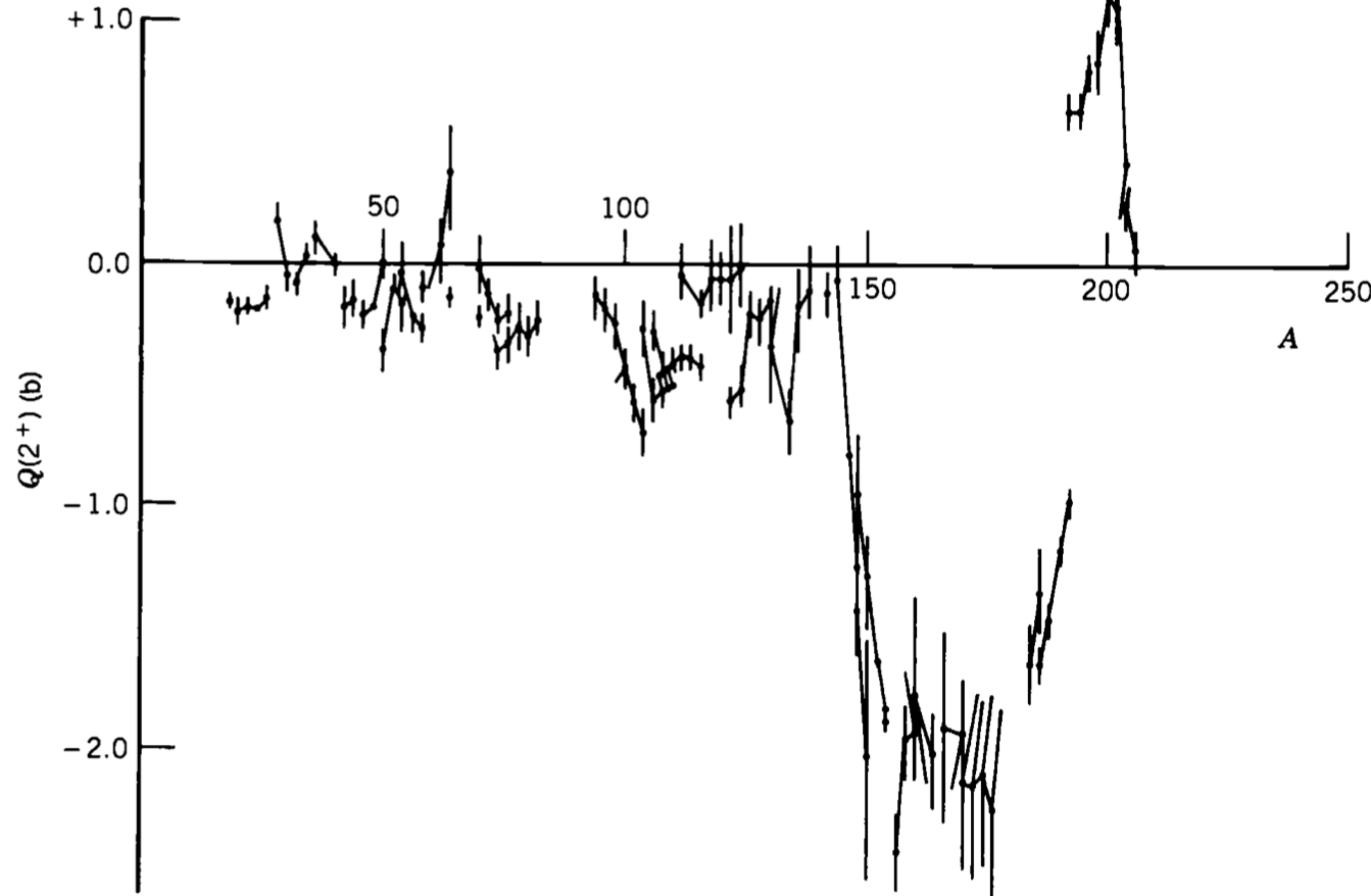


**Figure 5.16b** Electric quadrupole moments of lowest  $2^+$  states of even- $Z$ , even- $N$  nuclei. The lines connect sequences of isotopes.

# Liquid drop model

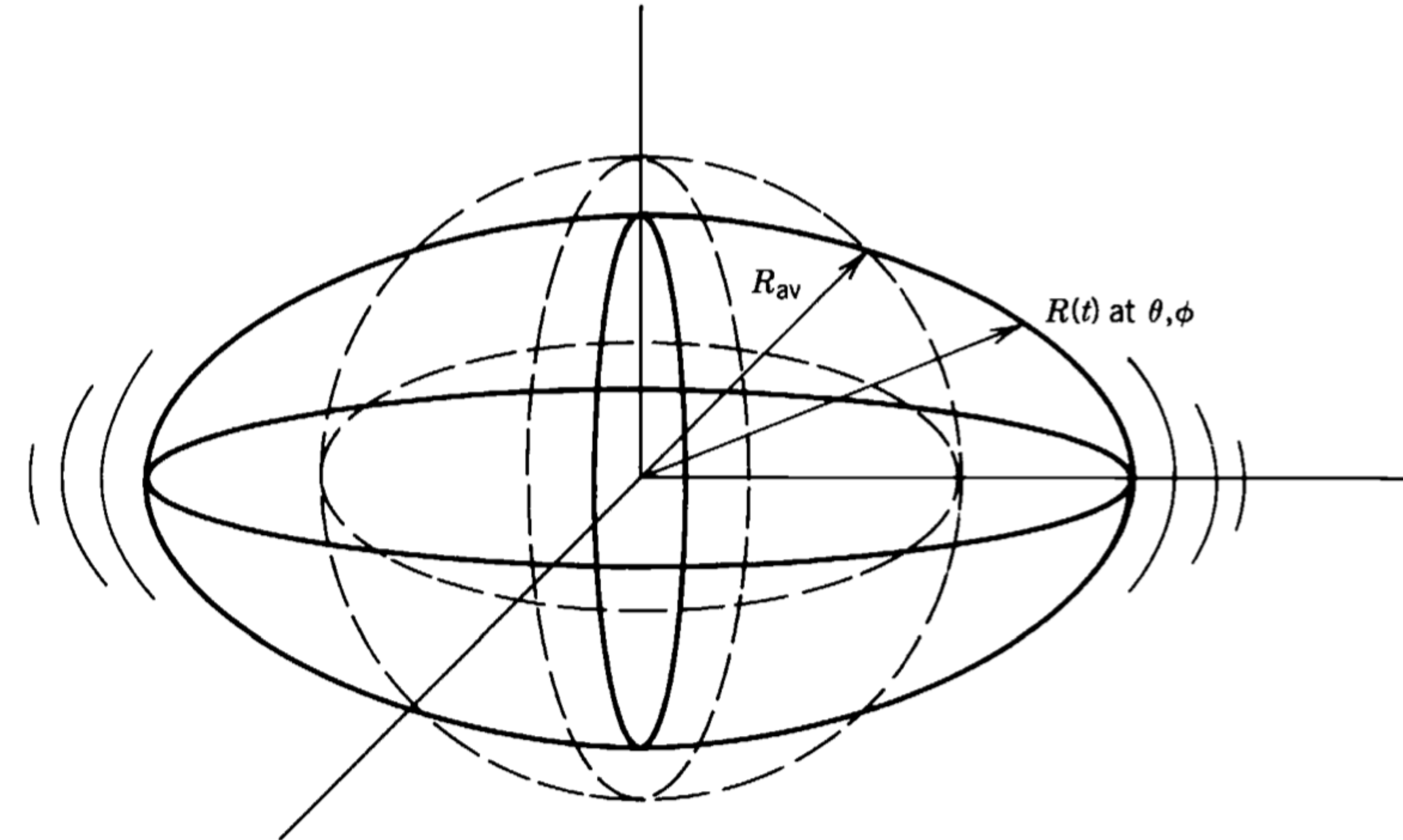


**Figure 5.17** A vibrating nucleus with a spherical equilibrium shape. The time-dependent coordinate  $R(t)$  locates a point on the surface in the direction  $\theta, \phi$ .



# Liquid drop model

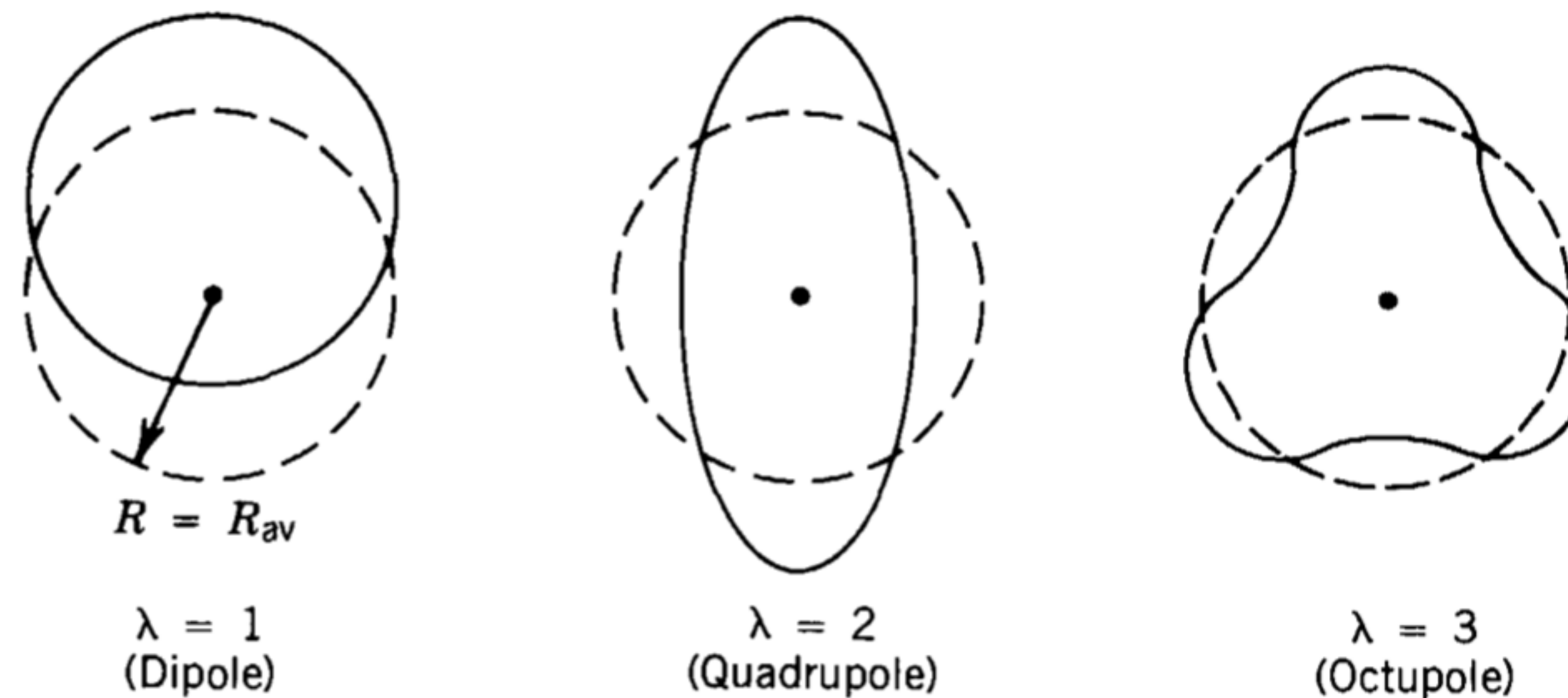


**Figure 5.18** The lowest three vibrational modes of a nucleus. The drawings represent a slice through the midplane. The dashed lines show the spherical equilibrium shape and the solid lines show an instantaneous view of the vibrating surface.

# Liquid drop model

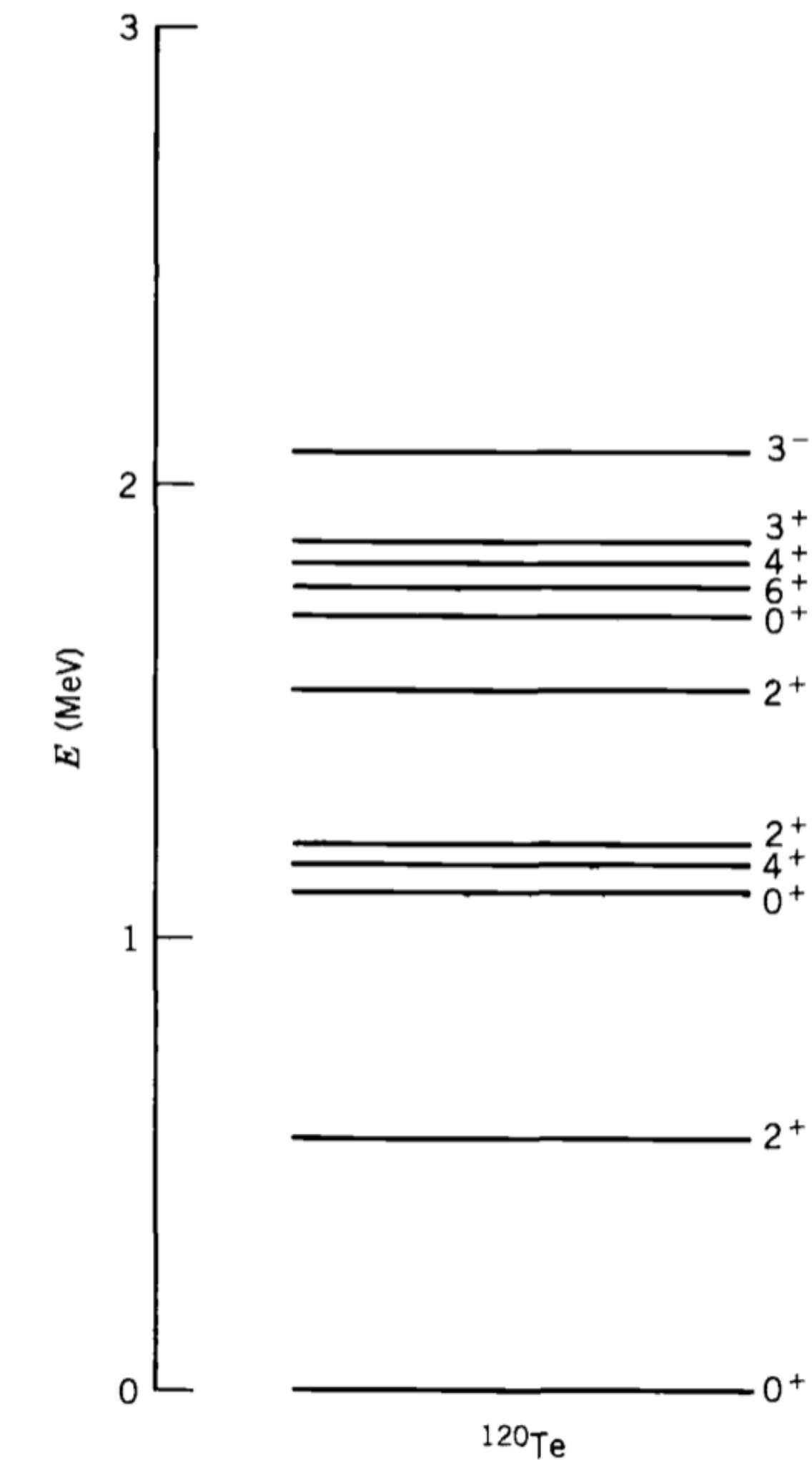


**Figure 5.19** The low-lying levels of  $^{120}\text{Te}$ . The single quadrupole phonon state (first  $2^+$ ), the two-phonon triplet, and the three-phonon quintuplet are obviously seen. The  $3^-$  state presumably is due to the octupole vibration. Above 2 MeV the structure becomes quite complicated, and no vibrational patterns can be seen.

# Liquid drop model

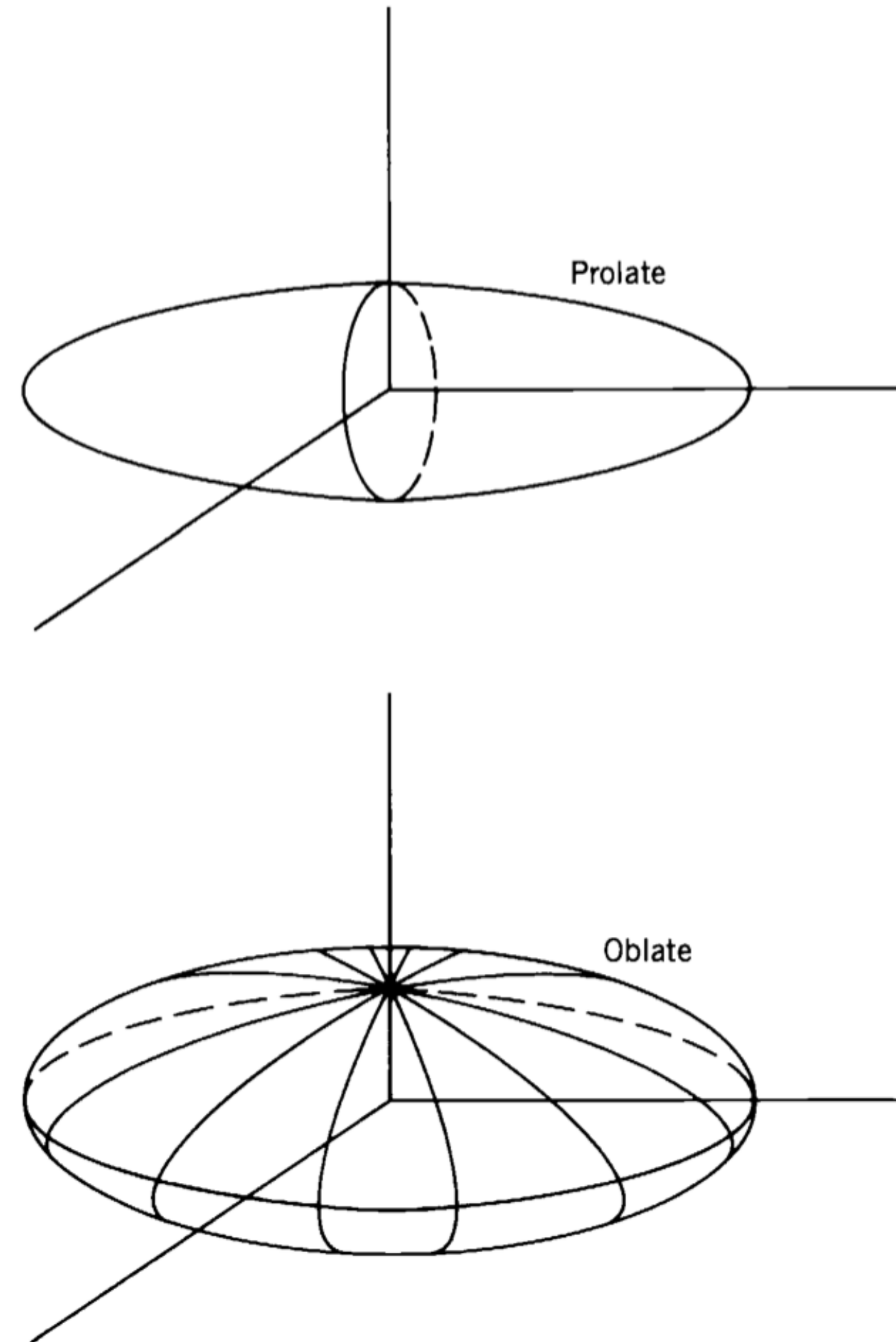


**Figure 5.20** Equilibrium shapes of nuclei with permanent deformations. These sketches differ from Figures 5.17 and 5.18 in that these do not represent snapshots of a moving surface at a particular instant of time, but instead show the static shape of the nucleus.

# Liquid drop model

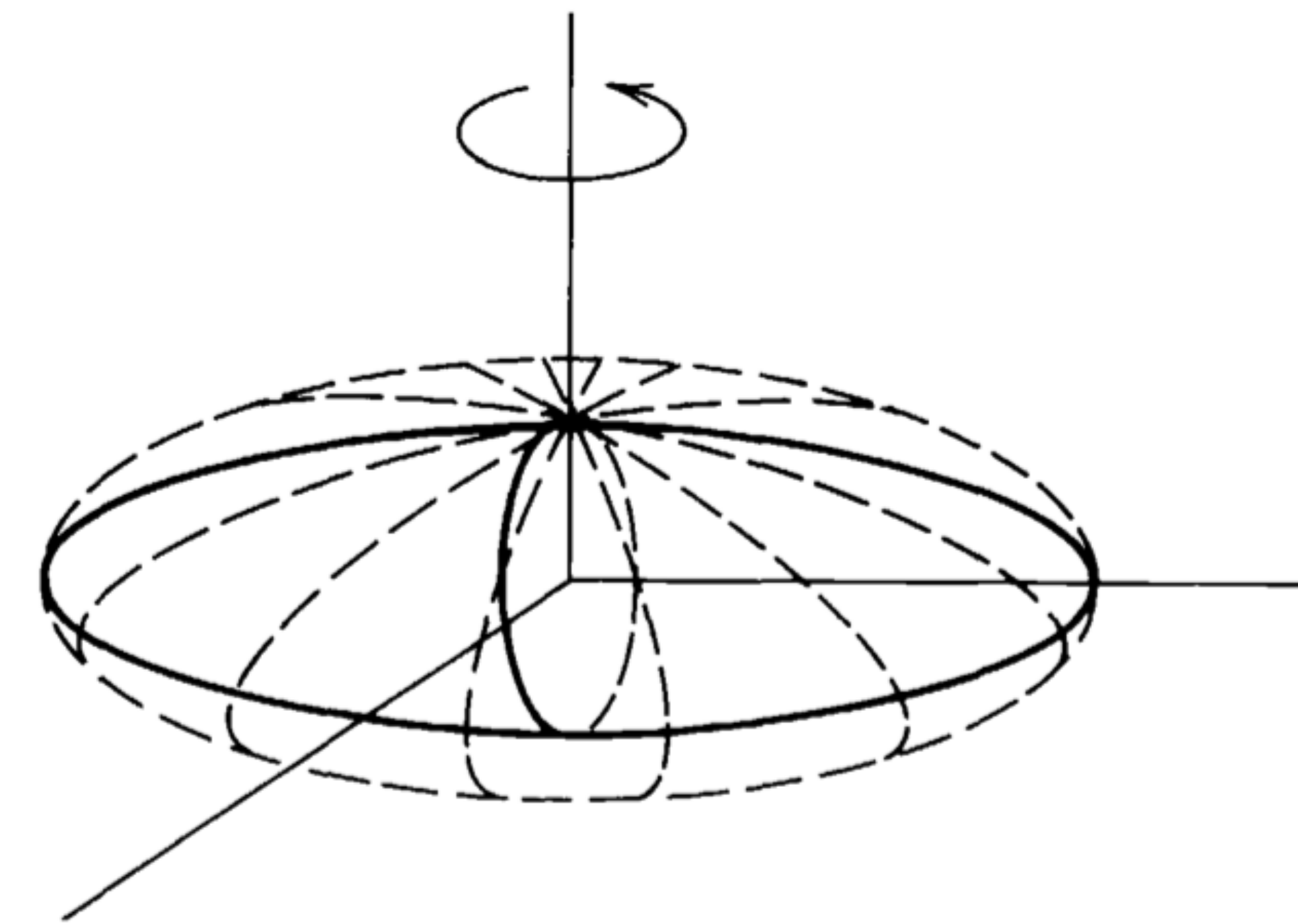


**Figure 5.21** Rotating a static prolate distribution about an axis perpendicular to its symmetry axis gives in effect a smeared-out oblate (flattened) distribution.

# Liquid drop model

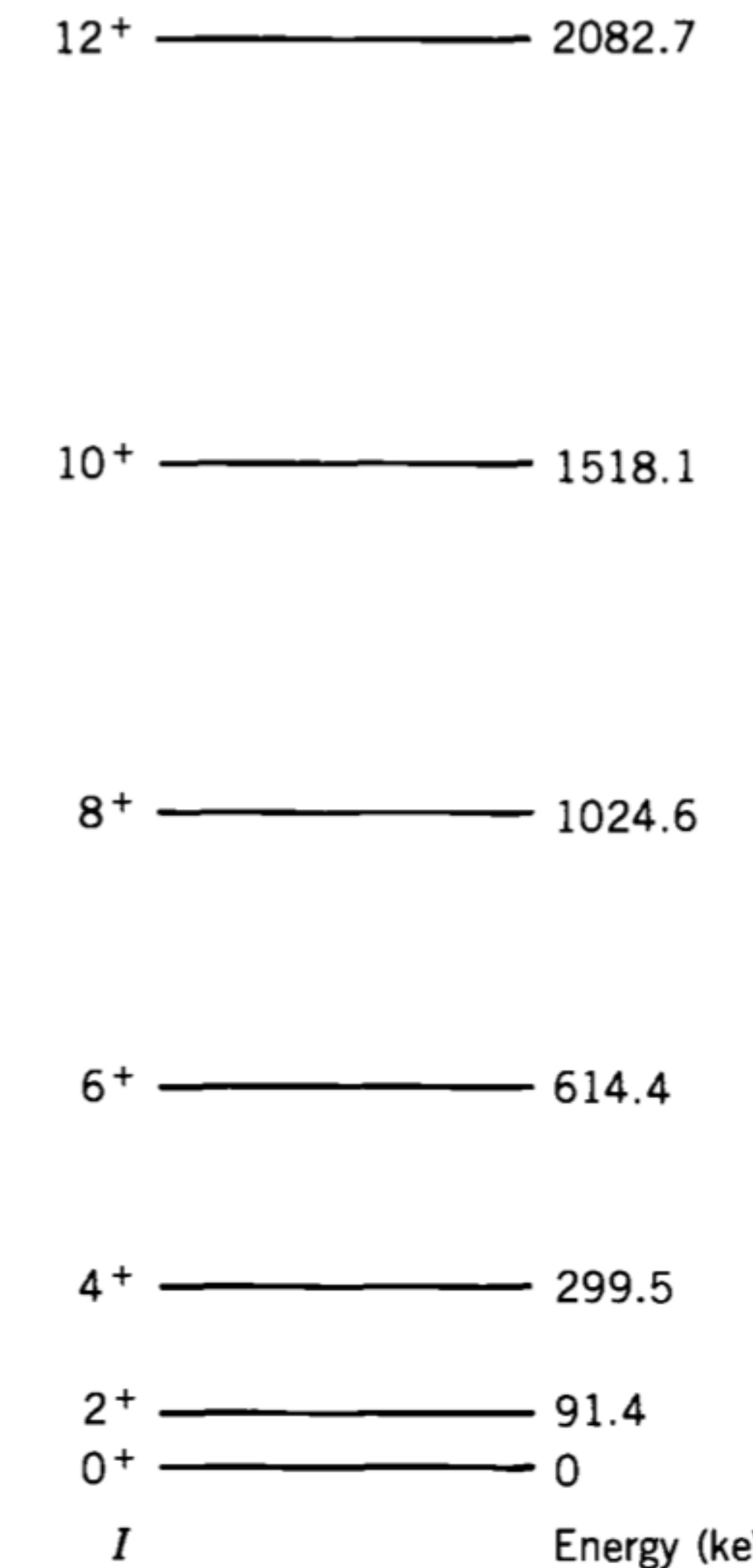


**Figure 5.22** The excited states resulting from rotation of the ground state in  $^{164}\text{Er}$ .

# Liquid drop model

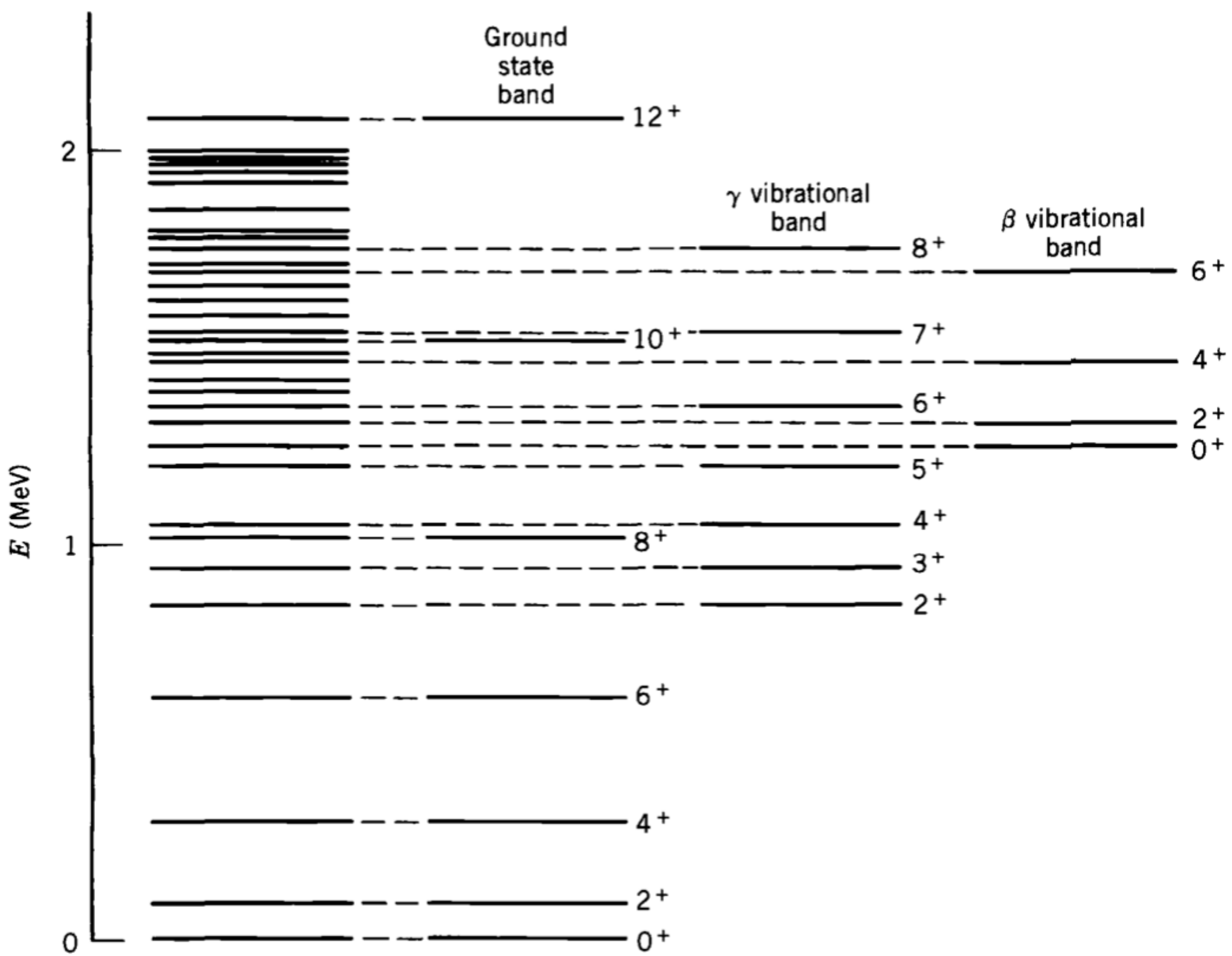


**Figure 5.23** The states of  $^{164}\text{Er}$  below 2 MeV. Most of the states are identified with three rotational bands: one built on the deformed ground state, a second built on a  $\gamma$ -type vibration (in which the surface vibrates transverse to the symmetry axis), and a third built on a  $\beta$ -type vibration (in which the surface vibrates along the symmetry axis). Many of the other excited states originate from pair-breaking particle excitations and their associated rotational bands.

# Liquid drop model

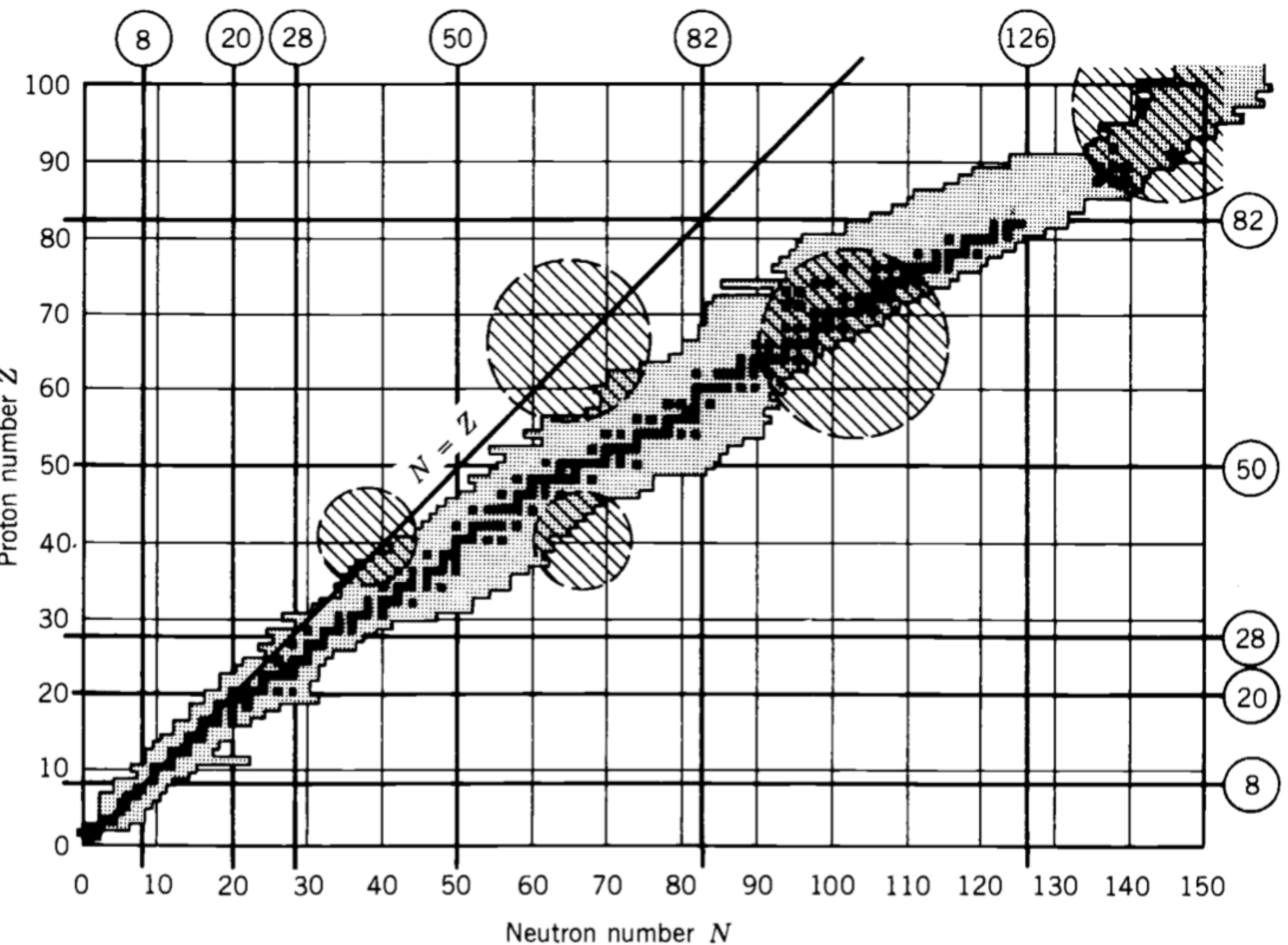


**Figure 5.24** The crosshatched areas show the regions far from closed shells where we expect that the cooperative effects of many single-particle shell-model states may combine to produce a permanent nuclear deformation. Such deformed nuclei have been identified in all of the regions where the crosshatched areas overlap the known nuclei.